Lead-free and lead-based ABO$_3$ perovskite relaxors with mixed-valence A-site and B-site disorder: Comparative neutron scattering structural study of (Na$_{1/2}$Bi$_{1/2}$)TiO$_3$ and Pb(Mg$_{1/3}$Nb$_{2/3}$)O$_3$

Wenwei Ge,[1,*] Christopher P. Devreugd,[1] D. Phelan,[2] Qinhui Zhang,[3] Muhtar Ahart,[4] Jiefang Li,[1] Haosu Luo,[3]
Lynn A. Boatner,[5] Dwight Viehland,[1] and Peter M. Gehring[2]

[1]*Department of Materials Science and Engineering, Virginia Polytechnic Institute and State University, Blacksburg, Virginia 24061, USA*
[2]*NIST Center for Neutron Research, National Institute of Standards and Technology, Gaithersburg, Maryland 20899-6100, USA*
[3]*Shanghai Institute of Ceramics, Chinese Academy of Sciences, Shanghai 201800, China*
[4]*Geophysical Laboratory, Carnegie Institution of Washington, Washington, D.C. 20015, USA*
[5]*Solid State Division, Oak Ridge National Laboratory, Oak Ridge, Tennessee 37831, USA*

We report the results of neutron elastic-scattering measurements made between $-250\,°C$ and $620\,°C$ on the lead-free relaxor (Na$_{1/2}$Bi$_{1/2}$)TiO$_3$ (NBT). Strong, anisotropic, elastic diffuse scattering intensity decorates the (100), (110), (111), (200), (210), and (220) Bragg peaks at room temperature. The wave-vector dependence of this diffuse scattering is compared to that in the lead-based relaxor Pb(Mg$_{1/3}$Nb$_{2/3}$)O$_3$ (PMN) to determine if any features might be common to relaxors. Prominent ridges in the elastic diffuse scattering intensity contours that extend along ⟨110⟩ are seen that exhibit the same zone dependence as those observed in PMN and other lead-based relaxors. These ridges disappear gradually on heating above the cubic-to-tetragonal phase transition temperature $T_{CT} = 523\,°C$, which is also near the temperature at which the dielectric permittivity begins to deviate from Curie-Weiss behavior. We thus identify the ⟨110⟩-oriented ridges as a relaxor-specific property. The diffuse scattering contours also display narrower ridges oriented along ⟨100⟩ that are consistent with the x-ray results of Kreisel *et al.* [Phys. Rev. B **68**, 014113 (2003)]; these vanish near $320\,°C$, indicating that they have a different physical origin. The ⟨100⟩-oriented ridges are not observed in PMN. We observe no equivalent relaxor-specific elastic diffuse scattering from the homovalent relaxor analogues K$_{0.95}$Li$_{0.05}$TiO$_3$ (A-site disordered) and KTa$_{0.95}$Nb$_{0.05}$O$_3$ (B-site disordered). This suggests that the ⟨110⟩-oriented diffuse scattering ridges are correlated with the presence of strong random electric fields and invites a reassessment of what defines the relaxor phase. We find that doping NBT with 5.6% BaTiO$_3$, a composition close to the morphotropic phase boundary with enhanced piezoelectric properties, increases the room-temperature correlation length along [1$\bar{1}$0] from 40 to 60 Å while doubling the associated integrated diffuse scattering. Similar behavior was reported by Matsuura *et al.* [Phys. Rev. B **74**, 144107 (2006)] for morphotropic compositions of PMN doped with PbTiO$_3$. Finally, we comment on the recent observation of monoclinicity in NBT at room temperature by placing a strict bound on the strength of the $(\frac{1}{2}\frac{1}{2}\frac{1}{2})$ superlattice reflection associated with the Cc space group based on the atomic coordinates published in the x-ray study by Aksel *et al.* [Appl. Phys. Lett. **98**, 152901 (2011)] for NBT. We show that a skin effect, analogous to that reported in the relaxors PZN-xPT and PMN-xPT, can reconcile our neutron single-crystal data with the x-ray powder data of Aksel *et al.* [Appl. Phys. Lett. **98**, 152901 (2011)]. Our finding of a skin effect in a lead-free, A-site disordered, heterovalent relaxor supports the idea that it arises in the presence of strong random electric fields.

I. INTRODUCTION

The ABO$_3$ perovskite compound (Na$_{1/2}$Bi$_{1/2}$)TiO$_3$ (NBT)[1] is an important A-site disordered material that, because it exhibits relaxor ferroelectric properties and is lead free, has been the subject of a fast-growing number of studies during the last decade. More significantly, NBT forms solid solutions with BaTiO$_3$ (NBT-xBT) that display both enhanced relaxor behavior and enhanced piezoelectric coefficients for compositions located on the rhombohedral side of the morphotropic phase boundary (MPB), which occurs around $x = 5 - 7\%$.[2–8] This situation is analogous to that seen in lead-based relaxors.[9] Given that the physical properties of lead-based relaxor ferroelectrics (RFs) are believed to be profoundly influenced by the underlying nanoscale structure, and in particular by the short-range correlated displacements of the Pb cations, we were motivated to examine the elastic diffuse scattering and crystal structure of a lead-free relaxor such as NBT over a broad temperature range using neutron scattering techniques

in an effort to clarify the origin of the diffuse scattering in lead-based RFs such as Pb(Mg$_{1/3}$Nb$_{2/3}$)O$_3$ (PMN) and Pb(Zn$_{1/3}$Nb$_{2/3}$)O$_3$ (PZN).

The extraordinary dielectric and electromechanical properties of B-site disordered, lead-based RFs and their solid solutions with PbTiO$_3$ (PT)[9–11] are believed by many researchers to be associated with randomly oriented, nanometer-sized regions of polar order known as polar nanoregions (PNR).[12–16] These PNR have been linked to the unique anisotropic and temperature-dependent x-ray and neutron diffuse scattering patterns that have been observed in lead-based RFs.[17–24] For example, in the (HK0) scattering plane, the elastic diffuse scattering intensity forms butterfly-shaped contours near reciprocal lattice vectors of the form (h00) that feature prominent ridges that extend along [110] and [1$\bar{1}$0], while the corresponding contours near (hh0) are ellipsoidal insofar as only a single ridge oriented along [1$\bar{1}$0] is seen. In general, the contours near all reciprocal lattice points in the (HK0) scattering plane exhibit ridges that extend along one or more

of the $\langle 110 \rangle$ directions.[25–28] The diffuse scattering in these compounds has been extensively studied and many different models have been proposed to explain the experimental data. Among these models, some assume (a) the presence of thin, pancake-shaped PNR,[21,29–31] (b) three-dimensional PNR for which the domain walls are parallel to $\{110\}$ crystallographic planes,[32] (c) correlated Pb displacements oriented along $\langle 110 \rangle$,[29,30,33] or (d) correlations between PNR embedded in an atomically disordered matrix (ADM).[34] But to date there is little consensus on its origin.[21,29,30,32–35] In 2006, Matsuura *et al.* made the interesting observation that the compositional dependence of the diffuse scattering in PMN-xPT correlates with that of the longitudinal piezoelectric coefficient d_{33}.[36] More specifically, the peak diffuse scattering intensity at the Brillouin-zone center ($q = 0$), the q-integrated diffuse scattering intensity, and the associated correlation length measured along $[1\bar{1}0]$ all increase rapidly as the system is doped towards the MPB,[36] which is where the piezoelectric coefficient d_{33} is largest.[9,11] This finding underscores the importance of developing a microscopic understanding of the diffuse scattering in relaxors, as it could be used to help design new relaxors and related materials with an even greater piezoelectric response.

NBT represents an intriguing counterpart to PMN and PZN because it is an *A*-site disordered RF, it contains no Pb cations, and yet solid solutions of NBT-xBT exhibit maximum electromechanical response for compositions located near an MPB just as happens with PMN-xPT and PZN-xPT.[2–8] Until recently, it was generally accepted that on cooling, NBT undergoes the following sequence of structural transitions: cubic (C, $Pm\bar{3}m$) $\xrightarrow{\sim 540^\circ C}$ tetragonal (T, $P4bm$) $\xrightarrow{\sim 260^\circ C}$ rhombohedral (R, $R3c$).[37,38] However, evidence of a monoclinic (M, Cc) structure under ambient conditions was reported by Gorfman *et al.* (in 2010) and Aksel *et al.* (in 2011).[39,40] Only a few studies concerning the local structure and origin of the relaxor behavior of NBT have been published.[41–45] X-ray diffraction studies by Kreisel *et al.* have revealed the existence of asymmetric "L"-shaped diffuse scattering intensity contours that display ridges extending along $\langle 100 \rangle$ on the low-Q (low-scattering angle) side of the Bragg peaks that vanish with increasing pressure.[42,44] A model of planar defects based on Guinier-Preston zones, in which correlated displacements of Na and Bi atoms occur along [100] within the R phase, was proposed to explain the existence of the asymmetric L-shaped contours.[42] Aleksandrova *et al.* (2006 and 2009) proposed that NBT is composed of PNR embedded in a nearly cubic matrix, and they detected evidence of a rhombohedral (R, $R3c$) phase via ^{23}Na NMR.[41,43] The sodium atoms within the PNR were suggested to be displaced along $\langle 111 \rangle$ and to have small shifts along the six possible $\langle 100 \rangle$ directions as well.[43] Very recently, Matsuura *et al.*[45] reported that the neutron diffuse scattering intensity around the (110) Bragg peak for NBT crystals grown under high O_2 pressure is weaker than that in crystals grown under normal atmospheric conditions, with the difference being attributed to an absence of Bi defects.

In this paper, we present an extensive characterization of the structural phase transitions that take place in NBT on cooling from the cubic phase by monitoring the temperature dependence of the fundamental Bragg peaks at (100) and (110)

as well as the superlattice reflections associated with the T ($P4bm$) and R ($R3c$) phases. We demonstrate that measurable $P4bm$ and $R3c$ static structural correlations coexist over a large temperature range spanning roughly 210 °C to 310 °C, which suggests that correlated tilts of the oxygen octahedra may play a seminal role in determining the long-range ordered structure of NBT. We shed light on the question of monoclinicity in NBT by reporting evidence of an anomalous skin effect in a lead-free, *A*-site disordered relaxor, for which the crystal structure of the near-surface or "skin" of the crystal differs from that of the bulk interior of the crystal. We next compare the neutron elastic diffuse scattering in NBT and PMN with that observed in two other *A*-site and *B*-site disordered perovskites, which have also been identified as relaxors but which, unlike NBT and PMN, are composed of homovalent cations. We find evidence of ridges of diffuse scattering in NBT that extend along $\langle 110 \rangle$, just as in PMN, which have not been observed before. These $\langle 110 \rangle$-oriented ridges of diffuse scattering are absent in the two homovalent perovskites, however, which suggests that strong random electric fields are an essential element in establishing the nanoscale structure of the lead-based RFs as well as the ultrahigh electromechanical response. Finally, we characterize the temperature-dependent diffuse scattering from single-crystal NBT and compare it with that from NBT-5.6%BT. We find that, as occurs for PMN-xPT,[36] the correlation length along $[1\bar{1}0]$ for NBT-5.6%BT (close to the MPB) is enhanced relative to that for pure NBT, while that along [100] is sharply diminished.

II. EXPERIMENTAL DETAILS

Several single crystals of NBT and NBT-5.6%BT were grown in air using a top-seeded solution growth (TSSG) method at the Shanghai Institute of Ceramics.[46] The Ba concentration in the as-grown condition was determined to be 5.6% using inductively coupled plasma atomic emission spectrometry (ICP-AES). Pseudocubic, $\langle 001 \rangle$-oriented crystals with dimensions of $3 \times 3 \times 0.7$ mm^3 were cut and platinum electrodes were deposited on the two largest (opposing) surfaces to allow for electrical measurements. Temperature-dependent dielectric permittivity data were measured using a multiple-frequency LCR meter (HP 4284A) on heating between 20 °C and 600 °C. The NBT lattice parameters were determined from the peak position and splitting of the pseudocubic (200) reflection measured using a Philips MPD high-resolution x-ray diffraction (XRD) system equipped with a two-bounce hybrid monochromator, an open three-circle Eulerian cradle, and a domed hot stage. A Ge (220)-cut crystal was used as an analyzer. The x-ray wavelength was that of Cu $K_{\alpha 1}$ (1.5406 Å), and the x-ray generator was operated at 45 kV and 40 mA. No information about the oxygen octahedral tilts could be obtained from these measurements because the relative intensities of the associated superlattice reflections are too weak to be measured by conventional XRD. A pseudocubic cell ($\sim 3.9 \times 3.9 \times 3.9$ Å) is used throughout this paper to index both the T and R phases following previous structural refinements by Jones and Thomas (2002).[38]

Neutron elastic-scattering measurements were performed on the BT4 and BT9 thermal-neutron triple-axis spectrometers located at the NIST Center for Neutron Research. Data

were taken with fixed incident and final neutron energies of 14.7 meV ($\lambda = 2.359$ Å); the (002) reflection from pyrolytic graphite (PG) crystals was used to monochromate and analyze the incident and scattered neutron beams. On BT4 (BT9), horizontal beam collimations of 40′-40′-sample-40′-240′ (40′-47′-sample-40′-80′) were used to measure the diffuse scattering. Substantially tighter beam collimations of 15′-47′-sample-10′-10′ were used on BT9 to better resolve any split Bragg peaks. PG filters were placed before and after the sample to eliminate higher-order harmonics in the incident and scattered neutron beams, respectively. The temperature dependence of the diffuse scattering in NBT was measured using the cold-neutron triple-axis spectrometer SPINS, also located at NIST, which provides superior wave-vector and energy resolution to that available on BT4 and BT9. On SPINS, the incident and final neutron energies were fixed at 5.0 meV ($\lambda = 4.045$ Å), and the effective horizontal beam collimations were 40′-80′-sample-80′-120′, resulting in an elastic energy resolution of 0.3 meV FWHM (full-width at half-maximum). A large NBT single crystal with dimensions $10 \times 10 \times 6$ mm^3 (3.54 grams) and {100} faces was cut from the crystal boule grown for this neutron diffuse scattering study. A smaller NBT-5.6%BT single crystal with dimensions $5 \times 5 \times 3$ mm^3 (0.44 grams) and {100} faces was cut from a different boule. The measured mosaic for both of these crystals above 550 °C was less than 0.30° FWHM. These crystals were mounted with either a [001] or [110] axis oriented vertically to provide access to Bragg reflections of the form (HK0) or (HHL) in the horizontal scattering plane, respectively. A closed-cycle ^{4}He refrigerator was used to access temperatures between -250 °C and 20 °C. A vacuum furnace was used to access temperatures between 20 °C and 620 °C. The room-temperature lattice constant of NBT is $a = 3.886$ Å; thus, 1 r.l.u. (reciprocal lattice unit) corresponds to $2\pi/a = 1.616$ Å^{-1}.

III. RESULTS

A. Long-range order: Structural phase transitions in NBT

Figure 1(a) shows the temperature dependence of the real part of the dielectric permittivity ε_r and the pseudocubic unit cell (200) d spacings, measured using x-ray diffraction, for the same ⟨001⟩-oriented single crystal of NBT on heating. Whereas the temperature-dependent x-ray diffraction data are consistent with the structural transformation sequence R $\xrightarrow{\sim 305 °C}$ T $\xrightarrow{\sim 540 °C}$ C, the permittivity measurements show no sign of the C → T transition at $T_{CT} \sim 540$ °C. This is consistent with previous studies and the claim that the C → T transition is a paraelectric → ferroelastic transition.[47,48] Instead, the permittivity data reveal an anomaly near $T_{max} = 320$ °C, where ε_r reaches a broad, flat maximum that is nearly frequency independent, a second anomaly near 305 °C where ε_r drops abruptly on cooling, and a third anomaly near $T_{RF} \sim 250$ °C, below which ε_r develops a weak frequency dispersion that is reminiscent of, but much smaller than, those in lead-based RFs.[49] The steep, nearly vertical drop in ε_r corresponds almost exactly to the T → R transition, which we identify via the splitting of the (200) Bragg peak at $T_{TR} \sim 305$ °C. We note that the transition temperatures determined with x rays are slightly higher than those previously reported for NBT powder
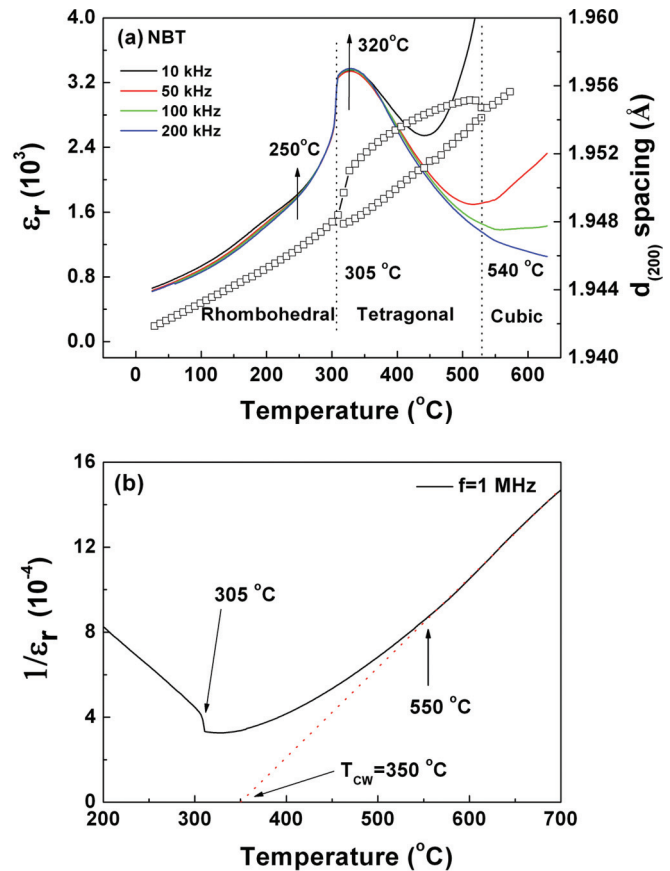

FIG. 1. (Color online) (a) Temperature dependences of the real part of the dielectric permittivity ε_r and the pseudocubic d spacing measured on an [001]-oriented single crystal of NBT while heating. The vertical dotted lines denote the structural transition temperatures determined from the splitting of the pseudocubic (200) Bragg peak measured via x-ray diffraction ($\lambda = 1.5406$ Å). (b) Temperature dependence of the inverse dielectric permittivity $1/\varepsilon_r$ measured at 1 MHz on heating. The red dashed line represents a Curie-Weiss fit extrapolated from high temperatures for which $T_{CW} = 350 \pm 0.7$ °C.

samples.[37,38] We also note that the nonlinear temperature dependence of the d spacings shown in Fig. 1(a) may be slightly exaggerated given that they were determined from just one Bragg peak and no corrections were made to account for any shift of the crystal scattering center during heating, but this does not affect any of the conclusions of our study. Figure 1(b) shows the inverse dielectric permittivity $1/\varepsilon_r$ measured at 1 MHz as a function of temperature. This frequency was chosen because ε_r exhibits an enhancement above 500 °C and below ~500 kHz that grows larger with decreasing frequency and can be attributed to an increased electrical conductance.[47] The dashed line is a Curie-Weiss fit ($T_{CW} = 350 \pm 0.7$ °C) extrapolated from high temperatures, and it indicates that ε_r deviates from Curie-Weiss behavior near 550 °C, which is at least 200 °C above T_{max}. The deviation from Curie-Weiss behavior occurs within the cubic phase of NBT as also happens with PMN.[50]

Neutron elastic-scattering data are presented in Fig. 2 that track the intensity, linewidth, and d spacing associated
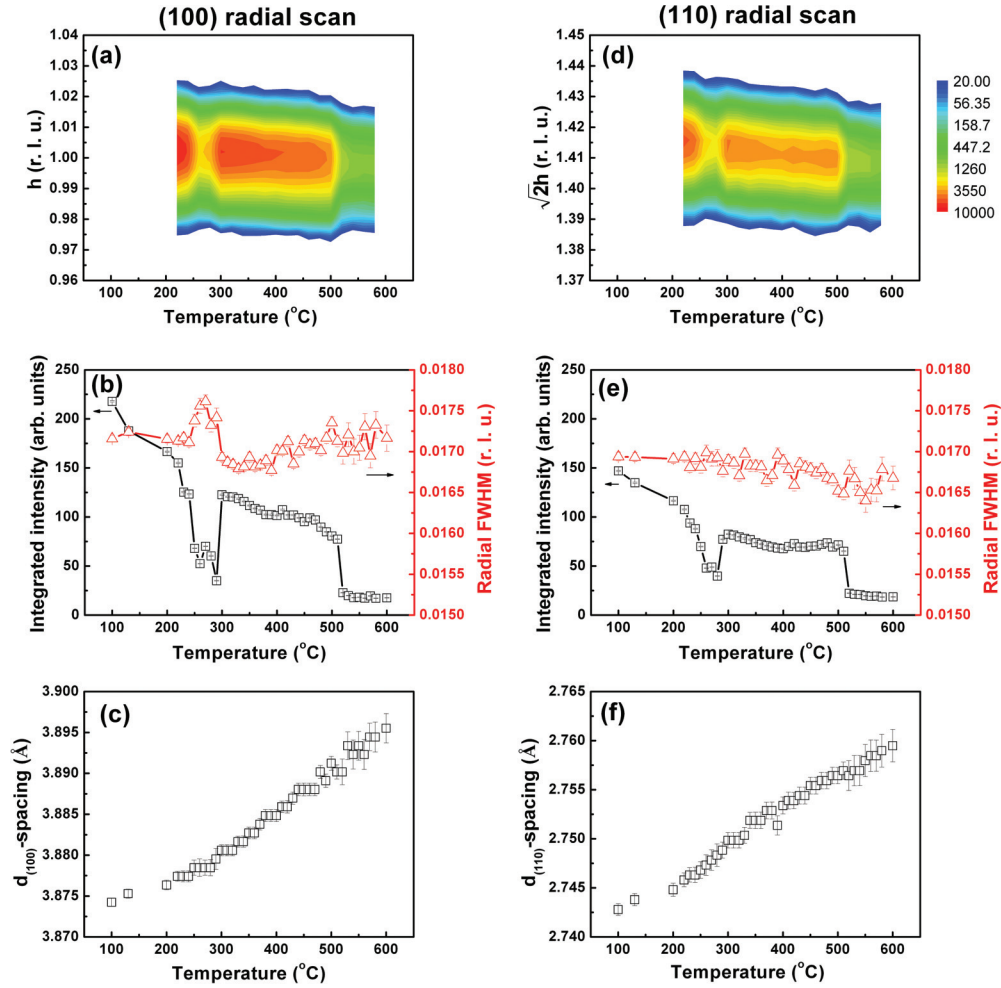
FIG. 2. (Color online) Temperature dependences of the radial linewidth, integrated scattered intensity, and *d* spacing associated with the (a)–(c) (100) and (d)–(f) (110) Bragg peaks, respectively. All data were measured on heating on BT9 using horizontal beam collimations of 15′-47′-sample-10′-10′. Note the logarithmic color intensity scale in panels (a) and (d). r.l.u.: reciprocal lattice units.

with the (100) and (110) Bragg peaks on heating from 100 °C to 600 °C. These parameters were extracted by fitting the Bragg-peak line shapes to Gaussian functions of the reduced wave vector $q = |\mathbf{Q} - \mathbf{G}|$, which is measured relative to the Bragg peak located at the reciprocal lattice vector $\mathbf{G}$, and where $\mathbf{Q}$ is the total scattering vector. The q resolution of these data is much coarser than that of the x-ray data shown in Fig. 1(a). Consequently, because the structural distortions in NBT are very small, no split peaks are seen, and only a single *d* spacing is shown in Figs. 2(c) and 2(f). Nevertheless, the C → T and T → R structural transitions are easily identified by the large release of extinction shown in Figs. 2(a), 2(b), 2(d), and 2(e) from which we estimate $T_{CT} \sim 515$ °C and $T_{RT} \sim 295$ °C. These values coincide reasonably well with the transition temperatures established with x rays in Fig. 1(a) even though these were determined using a different NBT crystal. The neutron scattering intensity was measured by scanning q along the radial direction (i.e., as in a $\theta - 2\theta$ scan), thus the (100) data reflect structural correlations along [100], while the (110) data reflect structural correlations along [110]. The structural transition near 305 °C is of particular interest because the linewidth along [100] broadens and then

narrows over a 50 °C-wide range below the T → R transition, whereas that along [110] remains comparatively flat. Indeed, the structural correlations along [110] are essentially independent of temperature within the limits of our instrumental q resolution. However, subsequent measurements of the (110) Bragg peak using finer collimations (better q resolution) show a comparatively muted dip in intensity and a strong increase in the linewidth along [110] below the T → R transition (data not shown). Also of interest are the large dips in both the (100) and (110) integrated intensities that are observed between 200 °C and 300 °C. As noted by Vakhrushev *et al.*,[51] this temperature range corresponds to that associated with the darkening of NBT crystals exposed to polarized light, also known as the "isotropization point," which is believed to occur due to the coexistence of short-range correlated regions of rhombohedral symmetry within the tetragonal phase (this coexistence is confirmed in Fig. 3). Measurements of the (110) Bragg-peak intensity on cooling from the cubic phase down to 127 °C, well within the rhombohedral phase, and then subsequently heating back into the cubic phase show no evidence of hysteresis for the C → T transition; however, the location of the large dip in the (110) integrated intensity shifts from 232 °C on
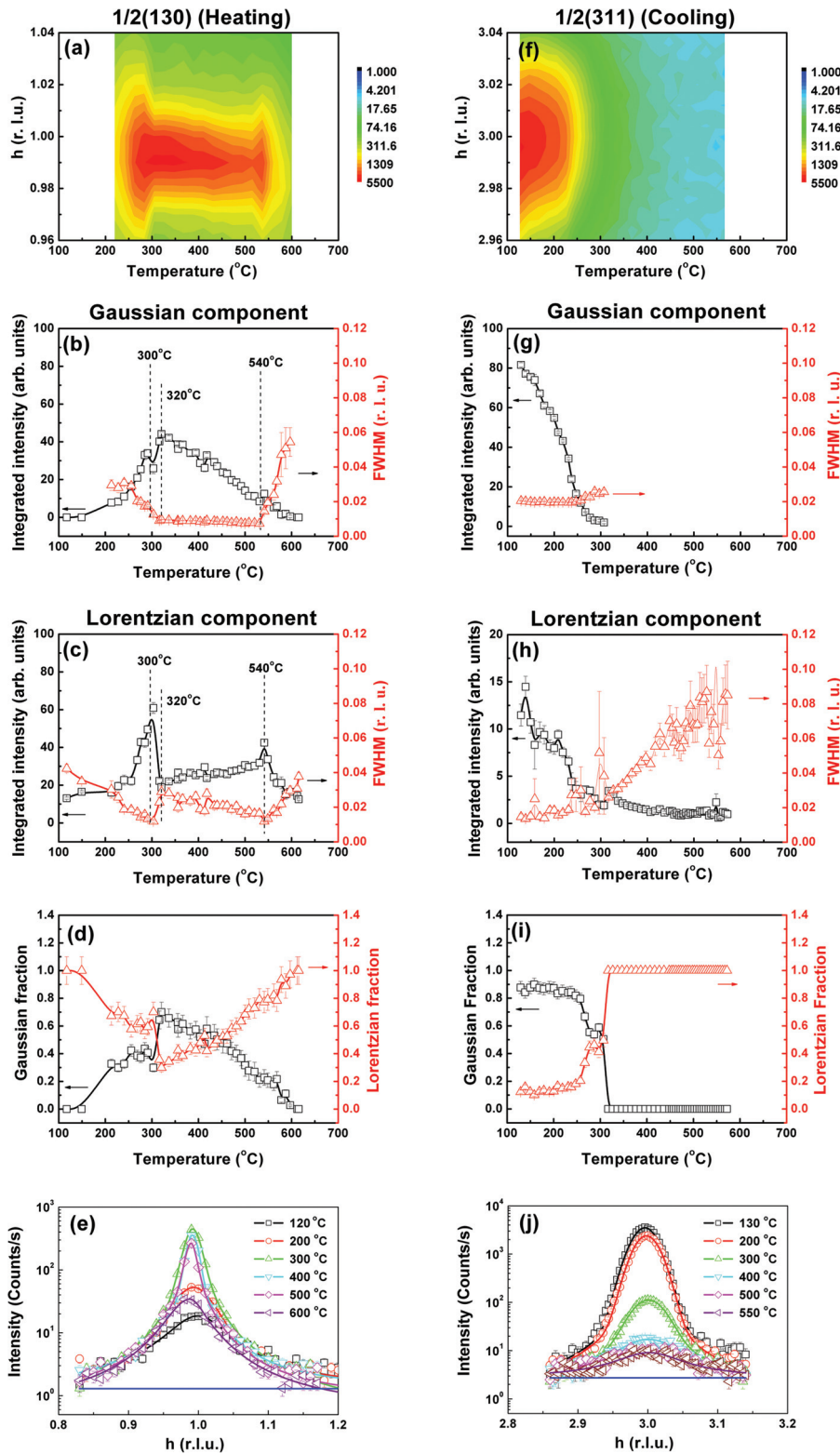
FIG. 3. (Color online) Temperature evolution of the (a)–(e) M-point superlattice peak at $\frac{1}{2}(130)$ and the (f)–(j) R-point superlattice peak at $\frac{1}{2}(311)$. The $\frac{1}{2}(130)$ data were measured on heating on BT9 using horizontal beam collimations of 15′-47′-sample-10′-10′. The $\frac{1}{2}(311)$ data were measured on cooling on BT4 using horizontal beam collimations of 40′-40′-sample-40′-120′. Note the logarithmic scales used in panels (a), (e), (f), and (j).

cooling to 258 °C on heating. This 26 °C shift may reflect the presence of some hysteresis associated with the isotropization point.

The tetragonal $P4bm$ and rhombohedral $R3c$ phases are signaled by the appearance of q-resolution-limited M-point and R-point superlattice reflections such as $\frac{1}{2}(130)$ and $\frac{1}{2}(311)$, respectively, which correspond to in-phase $(a^0a^0c^+)$ and an-

tiphase $(a^-a^-a^-)$ oxygen octahedral tilts (Glazer notation).[52] Figure 3 illustrates the evolution of the $\frac{1}{2}(130)$ (measured on heating) and $\frac{1}{2}(311)$ (measured on cooling) superlattice peak intensities and linewidths from 100 °C to 600 °C. The line shapes of both superlattice peaks were measured by scanning q along [100] and were fit to the sum of a Gaussian and Lorentzian function of q plus a temperature and q-independent

background term, which is given by

$$I_{\mathrm{diff}} = \frac{I_G}{\Gamma_G}\sqrt{\frac{\ln 2}{\pi}}\exp\left[-\ln 2\left(\frac{q-q_0}{\Gamma_G}\right)^2\right]$$
$$+ \frac{I_L\Gamma_L}{\pi\left[(q-q_0)^2+\Gamma_L^2\right]} + I_{\mathrm{back}}, \qquad (1)$$

where I_G (I_L) is the q-integrated scattering intensity of the Gaussian (Lorentzian) component, Γ_G (Γ_L) is the peak half width at half maximum (HWHM) for the Gaussian (Lorentzian) component, q_0 is the peak offset, and q is the reduced wave vector measured with respect to the Bragg peak; I_{back} is a temperature- and q-independent background.

This functional form was used because the superlattice peaks exhibit long tails over a large temperature range, even well below the T $\to$ R phase-transition temperature. These broad tails most likely reflect the critical fluctuations associated with the soft M_3 and R_{25} zone boundary modes, which have been studied by Vakhrushev *et al.*[51] Such fluctuations can be represented by a Lorentzian form, whereas the narrow component represents static Bragg scattering that is well-described by a Gaussian function of q. These line shapes were not convolved with the instrumental resolution function, thus the fitted q linewidths are broadened by the instrumental resolution. Figures 3(a) and 3(f) display the scattered neutron intensity on a logarithmic color scale at each (q,T) point, and the C $\to$ T and T $\to$ R structural transitions are evident. The corresponding values of the q-integrated intensity and the q linewidth, which we report in terms of the full width at half maximum (FWHM), are plotted for both the Gaussian and Lorentzian components as functions of temperature. We also show the relative Gaussian and Lorentzian contributions to the q-integrated intensities for each peak in Figs. 3(d) and 3(i). Anomalies in the integrated intensity and linewidth of both components of the $\frac{1}{2}$(130) reflection are seen near 300 °C, 320 °C, and 540 °C. The anomalies at 300 °C and 320 °C coincide well with those in the dielectric data shown in Fig. 1(a), while those at 300 °C and 540 °C coincide well with the changes in the d spacings measured with x rays. In addition, Fig. 3(b) shows that the linewidth of the Gaussian component is flat and resolution limited over the temperature range spanning the C $\to$ T and T $\to$ R structural phase transitions. Similarly, the integrated intensity of the Gaussian component of the $\frac{1}{2}$(311) peak shown in Fig. 3(g) does not appear until just above 300 °C, but then increases rapidly on cooling from 300 °C to 100 °C, signaling the transition into the rhombohedral phase. This is also reflected in the linewidth, which decreases on cooling until 260 °C, where it becomes constant and resolution limited. Another interesting feature of these data is illustrated in Figs. 3(c) and 3(h), where the Lorentzian components of both the M-point and R-point superlattice reflections are found to have measurable (nonzero) intensity over the entire temperature range, which are indicative of tetragonal and rhombohedral critical fluctuations, respectively. These data suggest that the corresponding soft M_3 and R_{25} modes must be confined to fairly low energies and/or quite broad in energy over the same range of temperatures because the instrumental energy resolution for the elastic measurements shown in Fig. 3 is only ~1 meV (FWHM). This is an intriguing observation because soft, broad zone-boundary modes at the M- and
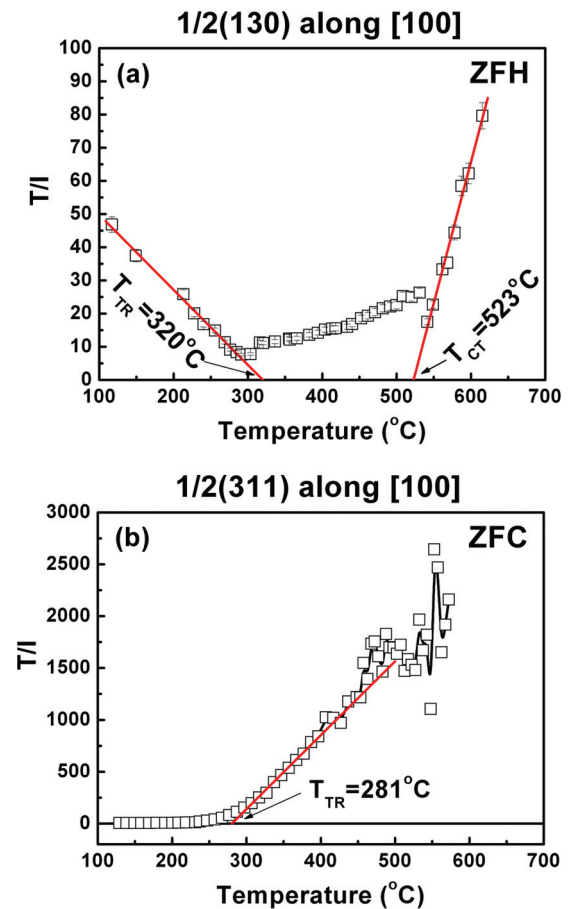

FIG. 4. (Color online) Curie-Weiss fits of the integrated intensities of the superlattice reflections at (a) $\frac{1}{2}$(310) and (b) $\frac{1}{2}$(311) from which the transition temperatures $T_{CT} = 523 \pm 2$ °C and $T_{TR} = 281 \pm 5$ °C (cooling) and $T_{TR} = 320 \pm 1$ °C (heating) were determined.

R-points of the cubic Brillouin zone have been observed in PMN by Swainson *et al.* who suggested that they could be a dynamical signature of the relaxor state.[53] A sharp onset of static (Gaussian) rhombohedral correlations is evident in Fig. 3(i) for the R-point superlattice reflection exactly at the T $\to$ R transition temperature. By contrast, static (Gaussian) tetragonal correlations appear to persist below the T $\to$ R transition, as shown in Fig. 3(d). This corresponds well to the region of the isotropization point mentioned earlier.

Following Vakhrushev *et al.*,[51] from the Curie-Weiss law we can fit the ratio (T/I) to a linear function of temperature, where I is the q-integrated intensity of the superlattice peak, to extract values for both T_{CT} and T_{TR}. These fits are shown in Fig. 4(a) for $\frac{1}{2}$(310) and Fig. 4(b) for $\frac{1}{2}$(311), from which we obtain $T_{CT} = 523 \pm 2$ °C, and $T_{TR} = 281 \pm 5$ °C (cooling) and $T_{TR} = 320 \pm 1$ °C (heating). The transition temperatures on cooling and heating for the T $\to$ R transition indicate a sizable hysteresis of the order of 40 °C, and appear to agree well with those observed by Vakhrushev *et al.*[51]

The data presented in Figs. 1–4 show that the dielectric anomalies and structural changes in NBT are directly related to changes in the $a^0a^0c^+$ in-phase and $a^-a^-a^-$ antiphase tilts of the oxygen octahedra. More importantly, they also demonstrate that the T $\to$ R transition is not a sharply defined phase bound-

ary. This is evident from the fact that the $\frac{1}{2}(310)$ reflection is still visible near 200 °C, although the linewidth is substantially larger than the instrument q resolution. This means that short-range tetragonal correlations (i.e., nanometer-scale tetragonal regions) associated with the in-phase tilt persist into the R phase at temperatures far below the R→T boundary at 300 °C. In fact, Figs. 3(b) and 3(g) prove that short-range ordered tetragonal regions persist far below $T_{TR} \sim 300$ °C. The size of these regions is inversely proportional to the linewidths of the superlattice peaks in q, which, because they were measured by scanning q along [100], correspond to the average extent over which these regions are spatially correlated along the [100] pseudocubic axis. A mixed state of long-range rhombohedral and short-range tetragonal correlations may be the cause of the frequency dispersion of the dielectric permittivity below 250 °C. On heating above 250 °C, the rapid decrease of the $\frac{1}{2}(310)$ linewidth and the increase of the integrated intensity indicate that the tetragonal regions are evolving into a long-range ordered T phase, and this appears to coincide with the vanishing of the dielectric frequency dispersion.

B. On the question of monoclinicity and the anomalous skin effect in NBT

In 2010, Gorfman and Thomas proposed that the crystal symmetry of NBT might be lower than $R3c$ at room temperature and possibly best described by the monoclinic space group Cc.[39] In 2011, high-resolution x-ray diffraction measurements of sintered powders of NBT by Aksel *et al.* revealed peak splittings that confirmed this proposition as well as the Cc space group.[40] Motivated by these results, we performed an extensive search for the $(\frac{1}{2}\frac{1}{2}\frac{1}{2})$ superlattice reflection that is allowed by the Cc structure but forbidden for $R3c$. Because this reflection results from correlated tilts of oxygen octahedra and is relatively weak, it is exceedingly difficult to observe using x rays (and effectively impossible using powders), but it should be readily visible via neutron diffraction from a bulk single crystal. We followed a standard procedure, described in early neutron studies of perovskites such as $SrTiO_3$,[54] in which long-wavelength (cold) neutrons are used to reduce the size of the Ewald sphere to eliminate the possibility of double scattering that could otherwise generate a false peak at $(\frac{1}{2}\frac{1}{2}\frac{1}{2})$; this method was recently used to prove that the ground-state crystal structure of PZT is not monoclinic Cc.[55]

In order to access the $(\frac{1}{2}\frac{1}{2}\frac{1}{2})$ reciprocal lattice point, the NBT crystal was aligned in the (HHL) scattering plane at room temperature on the SPINS cold-neutron spectrometer using neutrons of wavelength 4.045 Å (5 meV) so that both the (110) and (001) Bragg reflections could be oriented into the horizontal plane. The neutron wavelength was then changed to 5.222 Å (3 meV). At this wavelength, there can be no contribution from $R3c$-related superlattice peaks such as $\frac{1}{2}(311)$, as they all lie outside of the Ewald sphere. The same is true of all $P4bm$-related superlattice peaks such as $\frac{1}{2}(130)$, which is a concern because, as mentioned earlier, it still exhibits a nonzero intensity at room temperature. In fact, the only fundamental Bragg peak that can be reached at this wavelength is (001). Nitrogen-cooled beryllium filters were placed in both the incident and scattered neutron beams to minimize the presence of higher-order neutrons ($\lambda/2$, $\lambda/3$,
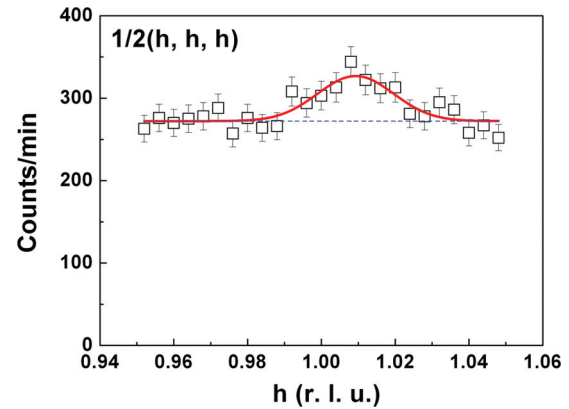

FIG. 5. (Color online) Room-temperature radial ($\theta - 2\theta$) scan measured through the $(^{1}/_{2}\,^{1}/_{2}\,^{1}/_{2})$ superlattice peak position. The weak peak is fit to a constant background plus a Gaussian function of q. Note the peak offset from $(^{1}/_{2}\,^{1}/_{2}\,^{1}/_{2})$. Error bars represent the square root of the number of counts. These data were measured on SPINS using horizontal beam collimations 50′-80′-sample-80′-120′ and incident and final neutron energies of 3 meV.

. . .) that would otherwise contaminate the incident beam scattered from the PG(002) monochromator. A nitrogen-cooled beryllium oxide filter was also placed in the incident beam because it provides a lower energy cutoff than does pure beryllium. In this configuration, there are no double-scattering processes available to contribute to any intensity measured at $(\frac{1}{2}\frac{1}{2}\frac{1}{2})$.

The fundamental (001) Bragg-peak intensity measured under these conditions was 36 000 counts/sec and nearly saturated the detector. By contrast, as shown in Fig. 5, an exceedingly weak peak was observed near $(\frac{1}{2}\frac{1}{2}\frac{1}{2})$ with an intensity of less than 1 count/sec (about 58 counts in 1 minute). This peak is also offset from the $(\frac{1}{2}\frac{1}{2}\frac{1}{2})$ reciprocal lattice position and is centered at $(\frac{1}{2}+\delta,\frac{1}{2}+\delta,\frac{1}{2}+\delta)$ where $\delta = 0.005$ r.l.u.; this offset is real as it is well outside our experimental uncertainty. These data were obtained by scanning q along [111] and are well-described by a Gaussian function with a linewidth roughly equal to the instrumental q resolution. In order to discern the origin of this weak peak, we calculated the expected ratio of the peak intensities $I(\frac{1}{2}\frac{1}{2}\frac{1}{2})/I(001)$, which is proportional to the ratio of the squares of the structure factors $|F(\frac{1}{2}\frac{1}{2}\frac{1}{2})|^2/|F(001)|^2$. Based on the atomic coordinates reported by Aksel *et al.*, the square of the structure factor for the $(\frac{1}{2}\frac{1}{2}\frac{1}{2})$ pseudocubic peak, which is a singlet in the Cc space group, is $|F(\frac{1}{2}\frac{1}{2}\frac{1}{2})|^2 = 4.01$, whereas that for the (001) pseudocubic peak, which is a doublet in Cc, has an average value $|F(001)|^2 = 560.4$. The ratio of the squared structure factors is then approximately 0.7%. (We have ignored the Debye-Waller factor, which is a small correction at low Q, as well as the Lorentz factor correction, which is only of order 5%.) If one also calculates, from the same Cc structural refinement, the d spacing of the monoclinic superlattice reflection in terms of that assuming a cubic structure, i.e., using the lattice constant determined from the cubic (001) Bragg reflection, then one finds that the $(\frac{1}{2}\frac{1}{2}\frac{1}{2})$ superlattice peak is shifted slightly to higher Q as observed, but only by $\delta = 0.001$ r.l.u.

Based on this analysis, we conclude that the crystal structure of *bulk* NBT at room temperature cannot be monoclinic Cc. Our experimentally measured peak intensity ratio $I(\frac{1}{2}\frac{1}{2}\frac{1}{2})/I(001) = 0.0027\%$ is more than 250 times smaller than that expected from the monoclinic Cc refinement of Aksel *et al.*, and our measured offset δ is five times too big. In fact, the measured Bragg peak intensity at (001) is almost certainly reduced by extinction effects, which are important for strong reflections in large single crystals such as ours; this suggests that the actual intensity discrepancy is even larger. We therefore confirm the average crystal structure of $R3c$, which is consistent with the neutron scattering study of Balagurov *et al.*[56] We cannot, however, simply dismiss the weak peak near $(\frac{1}{2}\frac{1}{2}\frac{1}{2})$. Because it cannot be explained by double scattering, we believe it is real and has some other origin. At the same time, we do not dispute the data or conclusions of Aksel *et al.* Rao *et al.* also report a room-temperature Cc structure for NBT, albeit one that coexists with an $R3c$ phase,[57] and the TEM study of Levin and Reaney supports the premise that the Cc symmetry of NBT is an averaged "best fit."[58] However, even using the atomic coordinates published by Rao *et al.*, our intensity discrepancy is nearly a factor of 200. We therefore propose that the two different room-temperature structures of NBT can be reconciled by the presence of a skin effect like that observed in the lead-based relaxors PZN, PZN-xPT, PMN, and PMN-xPT.[59–64] Given the large penetration depth of the neutron (relative to that for x rays), the scattering we observe should be dominated by the bulk of the crystal. There will, nevertheless, be a small contribution from the near-surface regions of our NBT crystal, which is large (having dimensions $10 \times 10 \times 6$ mm^3) and fully illuminated by the neutron beam. This near-surface or "skin" contribution could easily account for the very weak peak observed near $(\frac{1}{2}\frac{1}{2}\frac{1}{2})$; the larger than expected offset δ could be explained by the presence of strain in the near-surface region of the crystal. In fact, this offset (and the positive value of δ) is consistent with the skin effect observed by Xu *et al.* in PZN-xPT.[59,60] If a skin effect is present, then one should measure larger values of $I(\frac{1}{2}\frac{1}{2}\frac{1}{2})/I(001)$ for smaller crystals, as then the volume ratio of skin to bulk will be larger. We therefore repeated this cold-neutron measurement on a 0.02 gram single crystal of NBT and found a similar weak superlattice reflection for which $I(\frac{1}{2}\frac{1}{2}\frac{1}{2})/I(001) = 0.019\%$. This ratio is seven times larger than that measured on our large 3.54 gram NBT crystal (and likely much larger because of the aforementioned extinction effects). We also found the weak peak to be offset from $(\frac{1}{2}\frac{1}{2}\frac{1}{2})$ by a similar value of $\delta = 0.005$ r.l.u. We believe these findings represent clear evidence of a skin effect in the lead-free relaxor NBT.

C. Short-range order: Elastic diffuse scattering in NBT versus PMN

We now turn from our discussion of the average long-range structural order in NBT, which is defined by the Bragg peaks, to focus on the short-range structural order, which is manifested by the appearance of elastic diffuse scattering that is (by definition) broadly distributed in reciprocal space. Our goal is to compare the short-range order in NBT with that in PMN and other relaxors in order to determine which features (if any) might be universal. To this end, Fig. 6 provides an overview of

the reciprocal-space geometry of the elastic diffuse scattering intensity contours measured in the (HK0) scattering plane defined by the [100] and [010] pseudocubic crystallographic axes in three Brillouin zones for four different complex perovskite compounds: $K_{0.95}Li_{0.05}TaO_3$ (KLT 5%), NBT, PMN, and $KTa_{0.95}Nb_{0.05}O_3$ (KTN 5%). The left half of Fig. 6 shows data for KLT 5% and NBT, which are A-site disordered perovskites; the right half shows data for PMN and KTN 5%, which are B-site disordered perovskites. All four materials have been identified in the literature as relaxors, and only NBT exhibits any long-range ordered structural phase transitions on cooling.[65–67] In addition, whereas NBT and PMN are composed of heterovalent cations and thus possess relatively strong random electric fields (REFs), KLT 5% and KTN 5% are composed of homovalent cations and thus correspond to the weak REF limit. Thus, Fig. 6 provides data representative of the short-range structural correlations present near or well below T_{max} (the temperature at which the dielectric permittivity is maximum) for relaxors belonging to each of four distinct categories: (a) A-site disorder with weak REFs, (b) A-site disorder with strong REFs, (c) B-site disorder with weak REFs, and (d) B-site disorder with strong REFs. Figure 6 also provides information about the reciprocal-space geometry of the diffuse scattering from both high-symmetry planes (100) and (110) as well as from the lower-symmetry plane (210). All of the data in Fig. 6 were measured on BT4 (thermal neutrons) except those for KLT 5%, which were measured on SPINS (cold neutrons). All data have been plotted on a logarithmic intensity scale to better highlight the presence of any weak diffuse scattering; they have also been normalized to mass and counting time to facilitate a direct comparison between the four relaxor compounds.

The data for NBT and PMN, measured at room temperature, are displayed side by side in the middle of Fig. 6 for the (100), (110), and (210) Brillouin zones. These two compounds exhibit strong, highly anisotropic, elastic diffuse scattering contours in all zones that vanish at high temperatures (the temperature dependence is discussed in the next section). Analogous data for single-crystal KTN 5%, measured at $-263\,°C$, are displayed on the rightmost side of Fig. 6 for the same Brillouin zones. From Figs. 6(j)–6(l), it is immediately apparent that no such elastic diffuse scattering contours are visible in any of the three zones investigated. The only scattering present is that from the (100), (110), and (210) Bragg peaks [and from a powder ring that passes through (210) that should not be confused with diffuse scattering]. The data for KLT 5%, which are reproduced from Wakimoto *et al.*,[66] are shown on the leftmost side of Fig. 6. These data are more limited insofar as two-dimensional diffuse scattering contours were only available for the (110) zone. The contours shown in Fig. 6(b) bear some resemblance to those shown for NBT in Fig. 6(e). Figures 6(a) and 6(c) each show q scans measured at $-263\,°C$ and $-113\,°C$ along [100] through the (100) and (210) Bragg peaks, respectively, in which the scattered intensity is plotted on a logarithmic scale. These data show that the linewidth of each q scan is identical to that of the Bragg peak and independent of temperature, although some weak diffuse scattering may be present near (210). Thus, while some diffuse scattering from KLT 5% is evident near (110), it is absent near (100) and very weak near (210). This observation is important because it demonstrates that the structure factor
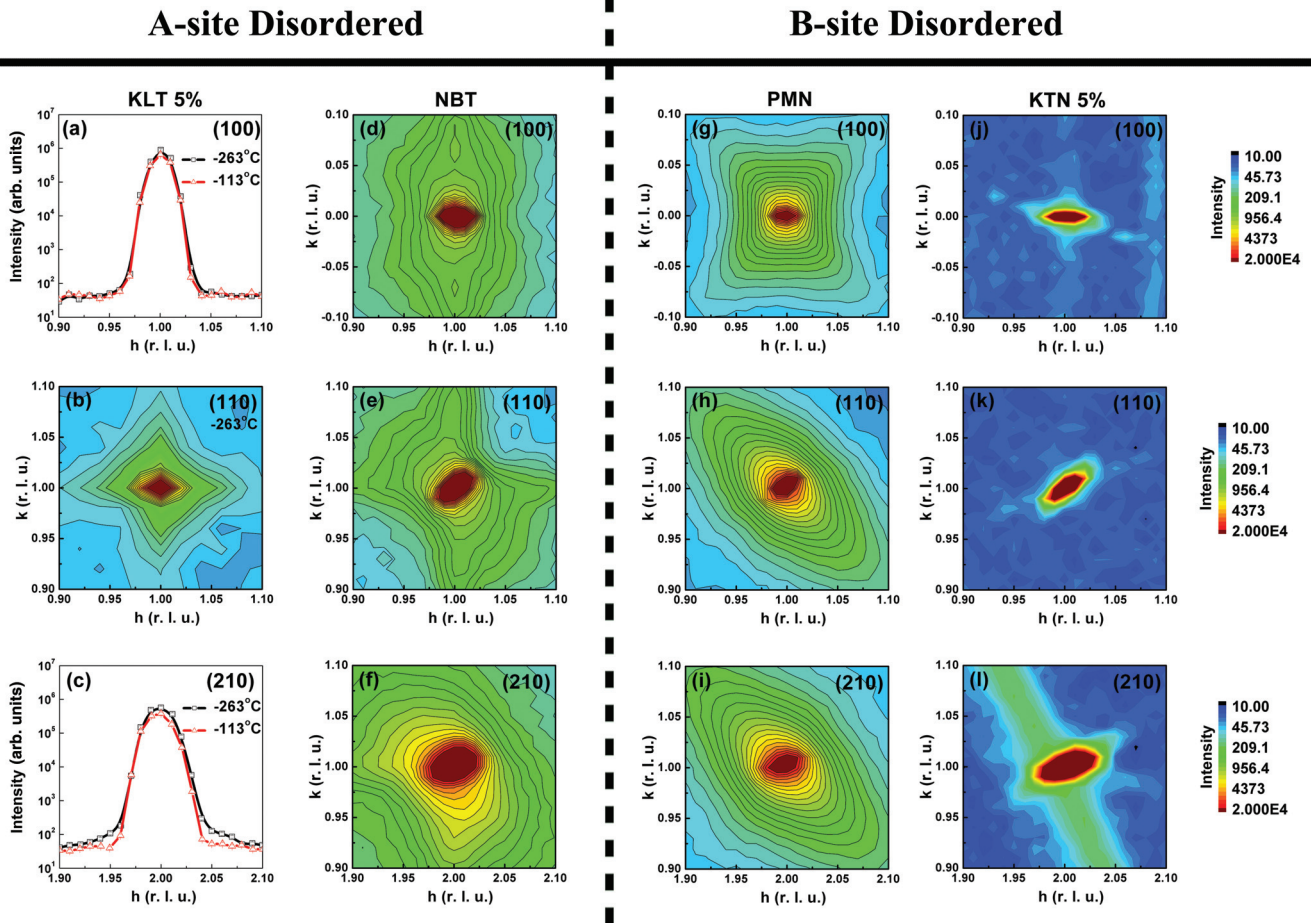
FIG. 6. (Color online) Comparison of the diffuse scattering intensity contours measured in the (HK0) scattering plane for four different complex perovskites in three different Brillouin zones. The data for $(K_{0.95}Li_{0.05})TaO_3$ were measured on SPINS. The other data were measured on BT4 and have been normalized to counting time. All data have been normalized to crystal mass. $(K_{0.95}Li_{0.05})TaO_3$ at -263 °C: (a) (100), (b) (110), and (c) (210); $(Na_{1/2}Bi_{1/2})TiO_3$ at 25 °C: (d) (100), (e) (110), and (f) (210); $Pb(Mg_{1/3}Nb_{2/3})O_3$ at 25 °C: (g) (100), (h) (110), and (i) (210); $K(Ta_{0.95}Nb_{0.05})O_3$ at -263 °C: (j) (100), (k) (110), and (l) (210). The $(K_{0.95}Li_{0.05})TaO_3$ data were kindly provided by Wakimoto *et al.* (from Ref. 66).

associated with the elastic diffuse scattering from KLT 5% differs markedly from that observed in lead-based, *B*-site disordered relaxors, for which the diffuse scattering near (100) and (210) is quite strong. In fact, Wakimoto *et al.* observe no diffuse scattering along either the [100] or [010] directions near (100) and (200).[66] A subsequent combined x-ray and cold-neutron scattering study by Wen *et al.* of single-crystal KLT 2%,[68] which is also considered to be a relaxor and exhibits no known long-range ordered structural phase transitions, found no evidence of any neutron elastic diffuse scattering near (100) or (110) between -263 °C and 27 °C. We therefore believe that the elastic diffuse scattering from KLT 5% near (110) shown in Fig. 6(b) is unrelated to the relaxor phase. Based on the stark differences illustrated in Fig. 6 between the elastic diffuse scattering observed from the heterovalent relaxors NBT and PMN and that observed from the homovalent relaxors KLT 5% and KTN 5% (which exhibit no elastic diffuse scattering of the type shown by NBT and PMN), it is extremely tempting to correlate the elastic, anisotropic, diffuse scattering in the lead-oxide relaxors with the presence of strong random

electric fields (REFs). Although the REFs are not necessarily zero in KLT or KTN (the cation off-centering will contribute to the REFs), they are certainly extremely weak in comparison to those in NBT and PMN.

Figures 6(g)–6(i) display the well-known elastic diffuse scattering intensity contours for PMN near (100) and (110) as well as less well-known contours for (210). These are consistent with the results of previous x-ray and neutron scattering studies.[17,26,69] As is the case with other lead-based, *B*-site disordered relaxors such as PZN,[21] PMT,[29] PST,[70] and PSN,[34] these contours can all be approximated by a superposition of one or more ellipsoidal distributions of diffuse scattering that are centered on each Bragg peak and oriented with the long axis aligned along $\langle 110 \rangle$.[21] Following the usage established by Xu *et al.* in Ref. 21, we shall henceforth refer to these ellipsoidal distributions as rods of diffuse scattering, which are consistent with the presence of planar (pseudo-two-dimensional) correlations having finite extent. By comparison, the corresponding contours for NBT are more complex. Figures 6(d)–6(f) clearly show that the

⟨110⟩-oriented ridges seen in the diffuse scattering contours for PMN are also present in those for NBT in all zones. Thus the short-range structural correlations associated with this diffuse scattering feature seem to be common to both $A-$ and B-site disordered relaxors, but they appear only when strong REFs are present. However, each panel also shows that the elastic diffuse scattering intensity from NBT exhibits additional (and narrower) ridges that extend from the Bragg peaks along ⟨100⟩; it is in this respect that the contours of KLT 5% and NBT appear somewhat similar. This additional feature indicates that the three-dimensional distribution of diffuse scattering from NBT is composed not only of ⟨110⟩-oriented rods, as in PMN and PZN,[21] but also of ⟨100⟩-oriented rods. Moreover, the ⟨100⟩-oriented rods exhibit a zone-dependent form factor (as do those oriented along ⟨110⟩) that governs the overall intensity. Near (100), the ⟨100⟩-oriented rods are only seen along $\pm$ [010] (transverse to **Q**); they are absent (or very weak) along $\pm$ [100] (parallel to **Q**). Near (110), however, these rods are clearly seen along both $\pm$ [010] and $\pm$ [100]. Finally, near (210), there is a strong asymmetry such that these rods are visible only on the low-Q sides of the Bragg peak, i.e., only for the [$\bar{1}$00] and [0$\bar{1}$0] directions. As first pointed out in the pioneering high-pressure, x-ray study by Kreisel *et al.*,[42] such asymmetric L-shaped diffuse scattering contours like those shown in Fig. 6(f) near (210) are reminiscent of those seen in Al-Cu metal alloys in which Guinier-Preston zones composed of Cu-rich regions form within {100} planes (in the Al-Cu alloy, however, the ⟨100⟩-oriented rods are present only on the high-Q side of the Bragg peaks).[71]

Our neutron data and those from the x-ray study by Kreisel *et al.* both reveal the presence of ⟨100⟩-oriented rods of diffuse scattering in NBT. However, the x-ray study reports no evidence of ⟨110⟩-oriented diffuse scattering rods in NBT that form the famous butterfly-shaped pattern near (100), but which are readily apparent from the neutron data we show in Figs. 6(d) and 6(e). The absence of such rods in the x-ray

study is evident from Figs. 1 and 2, respectively, of Ref. 42 and Ref. 72. This difference is easily understood if the x-ray scattering structure factor associated with the ⟨110⟩-oriented rods is much weaker in NBT than that in PMN. Kreisel *et al.* do report the presence of a [1$\bar{1}$0]-oriented diffuse scattering rod centered at (110); however, they identify this as thermal diffuse scattering. This assignment is logical because the coarse energy resolution of x-ray scattering will inevitably integrate over the scattering from low-energy phonons. However, as we are able to analyze the scattered neutron energies with an instrumental elastic energy resolution of 1 meV (FWHM), we can better discriminate elastic scattering from thermal diffuse scattering. Thus, we associate the ⟨110⟩-oriented rods of diffuse scattering that we observe with neutrons in all Brillouin zones with *static*, short-range ordered, structural correlations, not with thermal diffuse scattering. The fact that the intensity of these rods *decreases* with increasing temperature, which is demonstrated in the following section, supports our conclusion because thermal diffuse scattering *increases* with increasing temperature. Another difference between the x-ray study and our neutron study concerns the asymmetry of the ⟨100⟩-oriented diffuse scattering rods. In the x-ray case, these rods are reported to be visible only on the low-Q side of every Bragg peak. For example, near (100), only one ⟨100⟩-oriented rod is indicated, and it extends from the Bragg peak along [$\bar{1}$00]; near (110), two such rods are present, but these extend only along [$\bar{1}$00] and [0$\bar{1}$0], which results in the so-called asymmetric L-shaped contours. By contrast, our neutron data in Fig. 6(d) show ⟨100⟩-oriented rods extending from the (100) Bragg peak along both [010] and [0$\bar{1}$0], but there is no clear evidence of a rod along [$\bar{1}$00]. Near (110), shown in Fig. 6(e), we observe ⟨100⟩-oriented rods along all four directions: [100], [$\bar{1}$00], [010], and [0$\bar{1}$0]. The same is true for the contours measured near (200) and (220), which are shown in Figs. 7(a) and 7(b). Thus, the neutron elastic diffuse scattering intensity contours observed near reflections
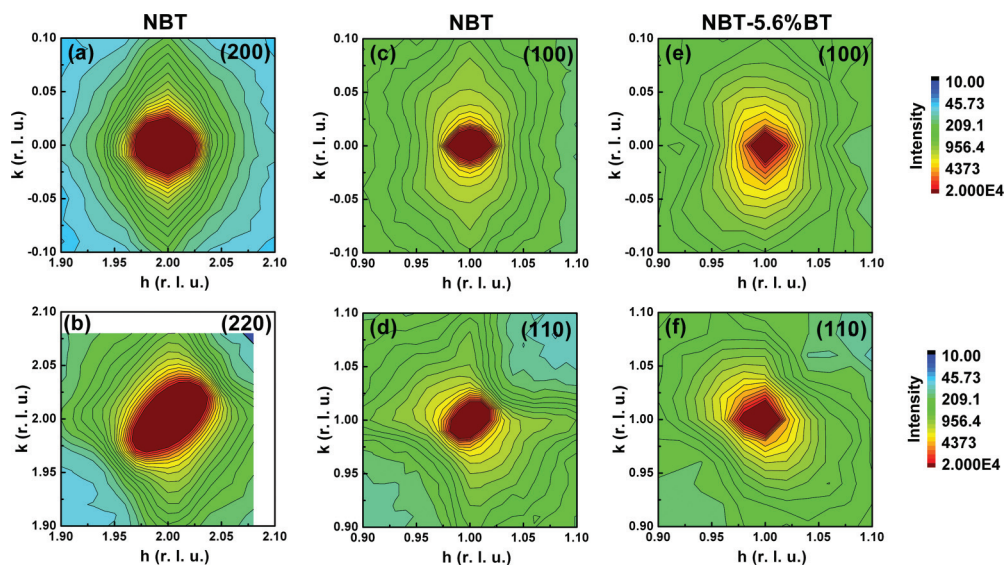

FIG. 7. (Color online) Diffuse scattering intensity contours measured in the (HK0) scattering plane for NBT near (a) (200), (b) (220), (c) (100), (d) (110), and NBT-5.6%BT near (e) (100) and (f) (110). All data were measured on BT9 at room temperature and normalized by mass and counting time.
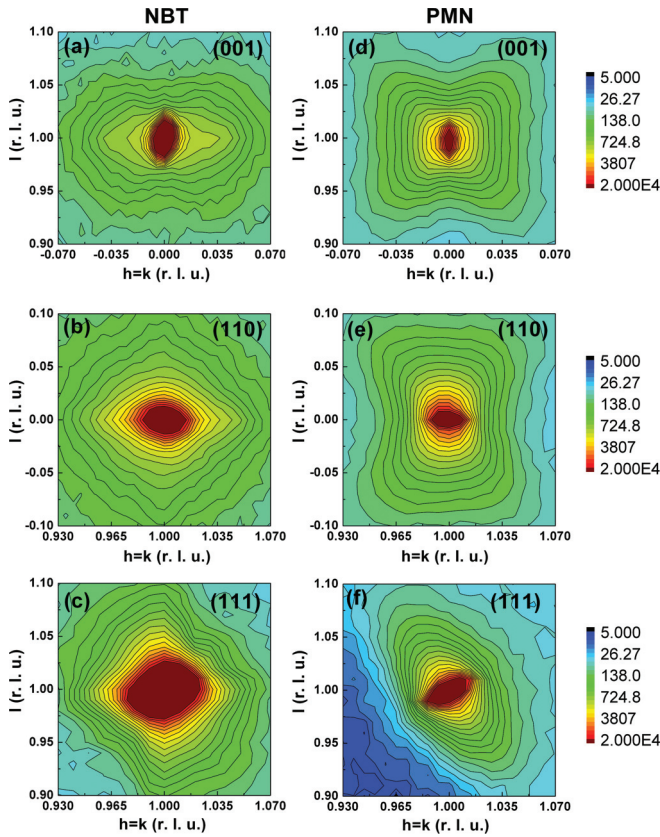
FIG. 8. (Color online) Diffuse scattering intensity contours measured at room temperature in the (HHL) scattering plane for NBT near (a) (001), (b) (110), and (c) (111) and for PMN near (d) (001), (e) (110), and (f) (111). All data were measured on BT4 and normalized by mass and counting time.

of the form (h00) and (hh0) are all symmetric insofar as they all exhibit twofold symmetry about the [001] axis perpendicular to the scattering plane. In the case of (210), shown in Fig. 6(f), the neutron and x-ray data agree, except that the $\langle 110 \rangle$-oriented elastic diffuse scattering rod is only observed with neutrons. It is important to note that our neutron data do not span a sufficiently large Q range to reveal the extremely broad lobes of diffuse scattering reported by Kreisel *et al.* that extend throughout the Brillouin zone, and which they interpreted as originating from a tendency for alternate, short rows of Bi- and Na-containing unit cells to occur in directions normal to $\langle 100 \rangle$.[42] We have, however, confirmed the presence of these diffuse scattering lobes using synchrotron radiation; this will be the subject of a future publication.

To better identify the similarities and differences between the nanoscale structures of NBT and PMN, we also present elastic diffuse scattering contours for both relaxors measured in the (HHL) scattering plane defined by the pseudocubic [110] and [001] crystallographic axes. These data, which are shown in Fig. 8, were measured at room temperature on BT4; they have also been normalized by mass and counting time to facilitate direct comparison and are displayed on a logarithmic intensity color scale. The diffuse scattering contours for PMN measured near (001) and (110), shown in Figs. 8(d) and 8(e), respectively, display a butterfly-shaped pattern and are consistent with the presence of $\langle 110 \rangle$-oriented rods of

diffuse scattering. As was shown by Xu *et al.* for the case of PZN-xPT,[21] these $\langle 110 \rangle$-oriented rods actually lie out of the (HHL) plane and thus are only visible because the out-of-plane component of the instrumental q resolution captures part of the diffuse scattering associated with these rods. It is also very important to note that none of the contours for PMN in Fig. 8 extends along $\pm$ [110]. In the pancake model of Xu *et al.*,[21] this is explained by assuming that the ionic displacements $\boldsymbol{\varepsilon}$ associated with disk-shaped polar nanoregions lie in the plane of the disk, i.e., they are orthogonal to the axis along which the correlation length is shortest. This assumption in conjunction with the expression for the diffuse scattering intensity, which is proportional to $(\mathbf{Q} \cdot \boldsymbol{\varepsilon})^2$, was then used to explain the systematic absences of some of the six $\langle 110 \rangle$-oriented rods near different Bragg peaks, which happens whenever the ionic displacements $\boldsymbol{\varepsilon}$ are perpendicular to $\mathbf{Q}$.

Given that the diffuse scattering contours for NBT in the (HK0) scattering plane near (100) are highly extended along directions transverse to the scattering vector $\mathbf{Q}$ (i.e., along [010] and [0$\bar{1}$0]) but not parallel to $\mathbf{Q}$ (i.e., along [100] or [$\bar{1}$00]), we should expect that the out-of-plane q resolution will also capture part of these out-of-plane $\langle 100 \rangle$-oriented rods in the (HHL) scattering plane, resulting in contours that are highly extended along $\pm$ [110] but not along [001]. As can be seen in Fig. 8(a), this expectation is correct. However, these same contours also bulge outwards diagonally from the Bragg peak just as they do for PMN. This feature is consistent with the NBT contours shown in the (HK0) plane and is further evidence of the presence of $\langle 110 \rangle$-oriented rods of diffuse scattering. The same reasoning can be used to explain the diffuse scattering contours in NBT near (110) and (111) shown in Figs. 8(b) and 8(c), respectively. Indeed, if the $\langle 110 \rangle$-oriented rods of diffuse scattering were not present, then the contours near (110) and (111) in the (HHL) scattering plane would simply resemble a cross, which is clearly not the case. We note that one could also argue that the *in-plane* $\langle 110 \rangle$-oriented rods of diffuse scattering are what cause all of the NBT contours in Fig. 8 to be highly extended along $\pm$ [110]. If true, then this would imply that the nanoscale structures responsible for the $\langle 110 \rangle$-oriented rods of diffuse scattering in NBT and PMN are significantly different. However, the contours near (111) shown in Fig. 8(c) show evidence of $\langle 110 \rangle$-oriented rods of scattering along only one diagonal, in agreement with the corresponding contours for PMN shown in Fig. 8(f). Moreover, the widths of the diffuse scattering ridges along $\pm$ [110] in Figs. 8(a)–8(c) are consistent with the narrower $\langle 100 \rangle$-oriented rods of diffuse scattering. Thus, based on all of the data shown in Figs. 6–8, we conclude that the nanoscale structures that generate the $\langle 110 \rangle$-oriented rods used to describe the reciprocal-space geometry in lead-based relaxors like PMN are the same as those we observe in the lead-free relaxor NBT, and thus are likely a relaxor-specific property. In addition, given that these $\langle 110 \rangle$-oriented rods of diffuse scattering are absent in the homovalent relaxors KLT 5% and KTN 5%, we speculate that they are generated only in the presence of sufficiently strong REFs. This observation also invites a reassessment of what defines the relaxor phase because the underlying physics responsible for the frequency dependence of the permittivity in PMN and NBT would then necessarily be entirely different from that in KLT.
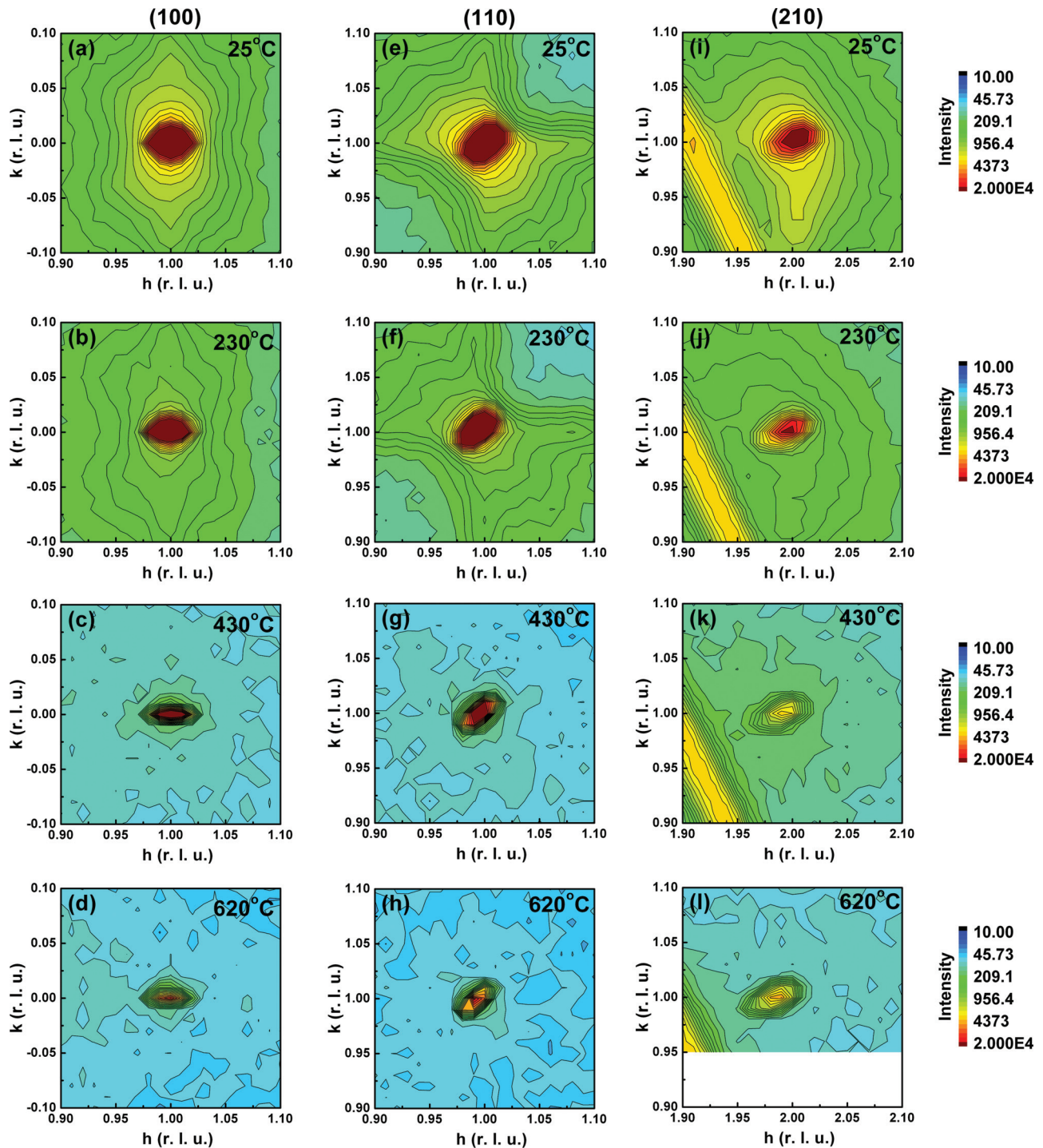
FIG. 9. (Color online) Diffuse scattering intensity contours for NBT measured in the (HK0) scattering plane near (100), (110), and (210) at 25 °C, 230 °C, 430 °C, and 620 °C. All data were measured on BT9. The narrow band in the lower left-hand corner of the data for (210) is a powder ring from the copper sample holder.

D. Temperature dependence of the elastic diffuse scattering in NBT

In this section, we examine the temperature dependence of the neutron diffuse scattering in NBT. All of the data presented in this section were measured on heating. Figure 9 shows the elastic diffuse scattering intensity contours for NBT measured in the (HK0) scattering plane near (100), (110), and

(210) at 25 °C, 230 °C, 430 °C, and 620 °C, respectively. With increasing temperature, the overall elastic diffuse scattering intensity clearly weakens, and at 430 °C, we observe only faint evidence of residual short-range correlations. At 620 °C, the temperature-dependent diffuse scattering is entirely gone, although there is (necessarily) some residual, temperature-independent diffuse scattering that remains due to substitutional disorder. The panels in Fig. 10 provide much greater
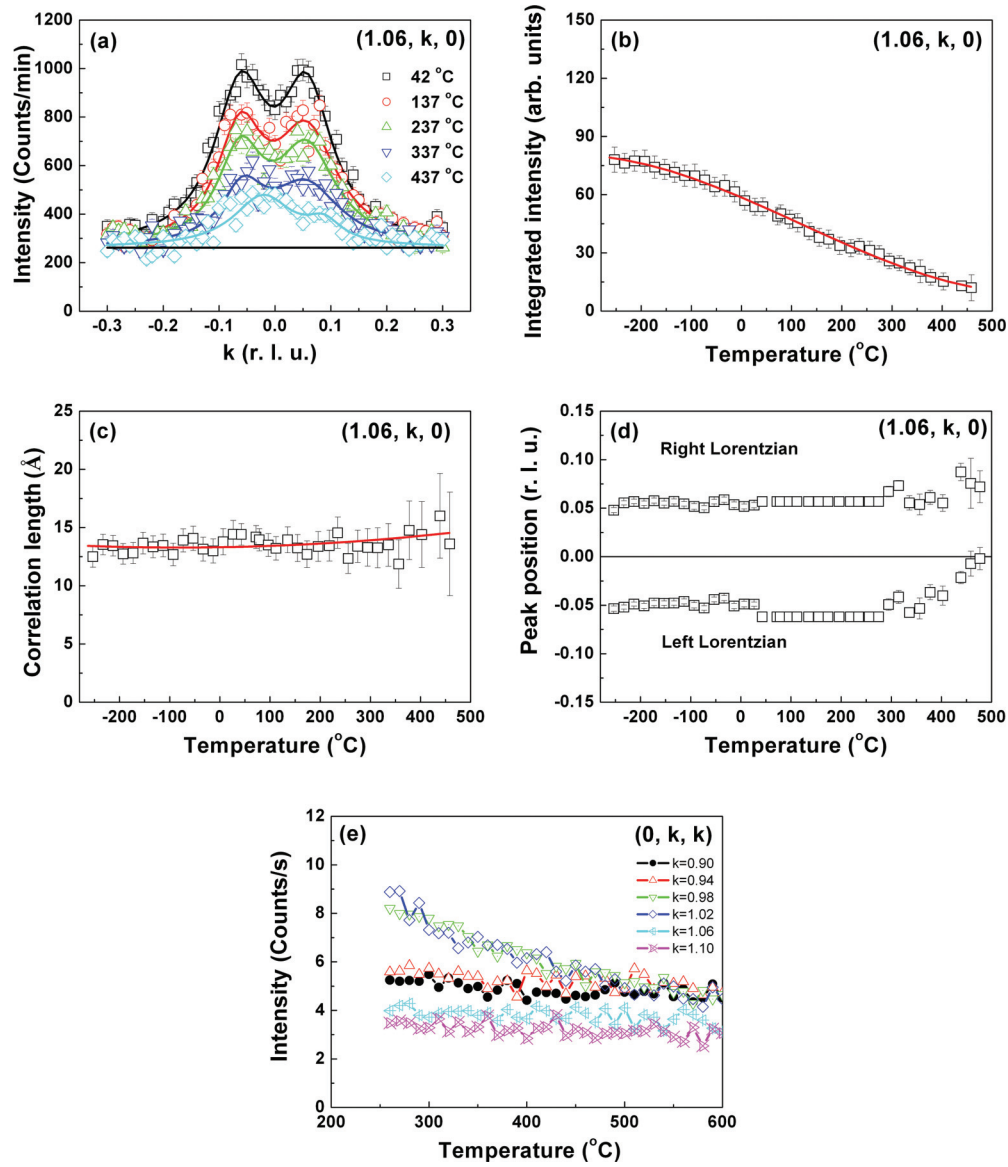
FIG. 10. (Color online) (a) Scan profiles of the diffuse scattering in NBT measured along $(1.06,k,0)$ at various temperatures. Solid lines represent fits to the sum of two equal-width Lorentzian functions of q plus a flat, temperature-independent background. Temperature dependence of the (b) q-integrated intensity, (c) correlation length, and (d) peak positions. Data shown in (a)–(d) were measured on BT4. (e) Plot of the diffuse scattering intensity measured on SPINS on cooling near (011) in the (HLL) scattering plane for various values of q using cold neutrons.

detail about how the short-range ordered structure of NBT melts. Figure 10(a) shows the evolution with temperature of q scans measured along the trajectory $(1.06,k,0)$, i.e., along [010] but offset from the (100) Bragg peak by 0.06 r.l.u. along [100]. This trajectory was chosen so that the q scans would probe the short-range structural correlations associated with the $\langle 110 \rangle$-oriented rods of diffuse scattering along [010] while avoiding both the $\langle 100 \rangle$-oriented rods and the Bragg peak. In order to characterize the diffuse scattering quantitatively, these scans were fit to the sum of two Lorentzian functions of q plus a flat, temperature-independent background, the results of which are indicated by the solid lines. Each Lorentzian function was parameterized by the formula

$$I_{\text{diff}} = \frac{I_0\Gamma}{\pi[(q-q_0)^2 + \Gamma^2]}, \qquad (2)$$

where I_0 is the q-integrated diffuse scattering intensity, $\Gamma = 1/\xi$ is the peak half width at half maximum (HWHM), i.e., the inverse of the real-space correlation length ξ, q_0 is the peak offset, and q is the reduced wave vector measured with respect to the Bragg peak. The Lorentzians were constrained to have the same linewidth Γ, but all remaining parameters were allowed to float. Figure 10(b) shows the temperature dependence of the associated q-integrated diffuse scattering, which decreases gradually and monotonically with increasing temperature. By contrast, the correlation length ξ measured along [010] is effectively temperature independent, as shown in Fig. 10(c). Likewise, the peak positions of the two Lorentzians, plotted in Fig. 10(d), are also temperature independent and displaced symmetrically about $k = 0$ by 0.06 r.l.u. The 0.06 r.l.u. offset proves that these ellipsoidal rods of diffuse scattering are indeed oriented exactly along $\langle 110 \rangle$. It is only
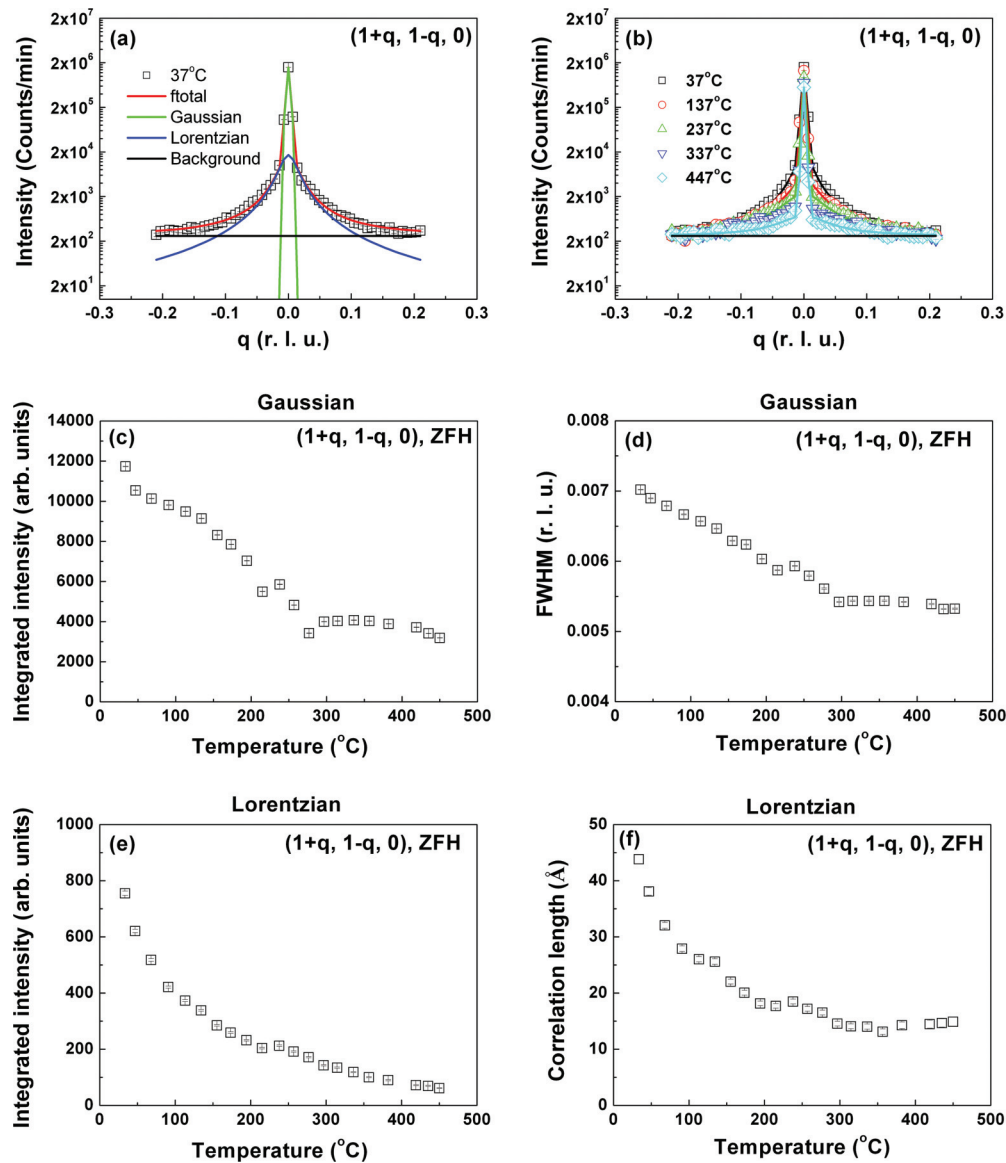
FIG. 11. (Color online) (a) Scan profile of the diffuse scattering in NBT measured along $(1+q, 1-q, 0)$ at 37 °C. Solid lines represent the total (red) and individual components of the fitting profile (Gaussian, Lorentzian, and a flat, temperature-independent background). (b) Scan profiles and fits are shown for a range of temperatures. Temperature dependence of the (c) Gaussian integrated intensity, (d) Gaussian linewidth (FWHM), (e) Lorentzian integrated intensity, and (f) correlation length along $[1\bar{1}0]$. All data were measured on BT4.

above ∼400 °C that the peak positions of the Lorentzians begin to shift towards $k = 0$. These data are consistent with the eventual disappearance of the diffuse scattering near or at $T_{CT} = 523$ °C. However, as was shown in PMN,[20] the temperature dependence of the diffuse scattering in the lead-based relaxors can vary strongly when measured with an elastic energy resolution (HWHM) greater than 0.25 meV. For this reason, cold-neutron diffuse scattering data measured near (011) on SPINS, which provides an elastic energy resolution HWHM of 0.15 meV, are shown in Fig. 10(e), and these data confirm that the temperature at which the diffuse scattering vanishes is effectively indistinguishable from T_{CT}. But because the diffuse scattering intensity varies so weakly with temperature near T_{CT}, we cannot pinpoint the temperature at which it vanishes more accurately than 525 ± 25 °C.

We performed a similar analysis of q scans measured along the trajectory $(1+q, 1-q, 0)$ that pass directly through the (110) Bragg peak, which were chosen to probe the short-range structural correlations associated with the ⟨110⟩-oriented rods of diffuse scattering along the $[1\bar{1}0]$ direction. In this case, the scans were fit to the sum of a single Lorentzian function (with $q_0 = 0$) to describe the ⟨110⟩-oriented rods, a much narrower Gaussian function (to describe the Bragg peak), and the same flat, temperature-independent background. The results of this analysis are shown in Fig. 11, where Fig. 11(a) illustrates the individual components of the fitting profile at 37 °C, and Fig. 11(b) shows the quality of the fits over a range of temperatures. Figures 11(c) and 11(d) show how the integrated intensity and linewidth (FWHM) of the Gaussian component (Bragg peak) vary with temperature; both exhibit a change in slope in the vicinity of the T → R structural phase-transition
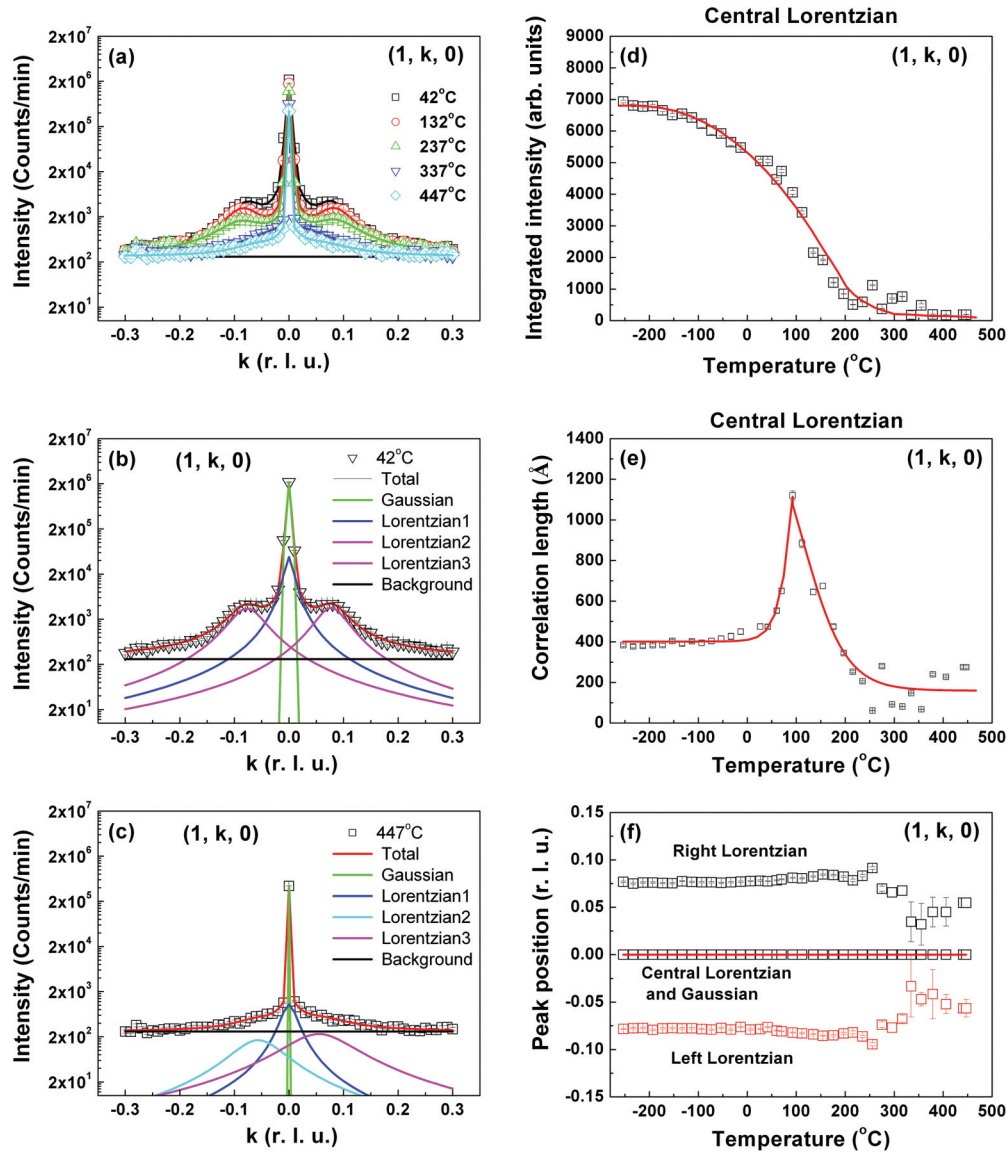
FIG. 12. (Color online) (a) Scan profiles of the diffuse scattering in NBT measured along $(1,k,0)$ at various temperatures. Solid lines represent fits to a Gaussian, three Lorentzians, and flat, temperature-independent background. Scan profile and individual fitting components are shown at (b) 42 °C and (c) 447 °C. Temperature dependence of the (d) central Lorentzian integrated intensity, (e) central Lorentzian correlation length along [010], and (f) peak positions of the Lorentzian and Gaussian components. All data were measured on BT4.

temperature on heating. Figure 11(e) displays the temperature dependence of the integrated intensity associated with the Lorentzian component used to model the $\langle 110 \rangle$-oriented rods of diffuse scattering, and we observe the same temperature dependence as in Fig. 10(b), where the correlations were being probed along [010]. What is most striking, however, is that the correlations measured along [1$\bar{1}$0], shown in Fig. 11(f), are strongly temperature dependent. This is a stark contrast to the temperature-independent behavior displayed by the short-range structural correlations measured along [010] shown in Fig. 10(c). It is also interesting to note that the limiting high-temperature value of the correlation length in both cases is close to 15 Å.

Having characterized the temperature dependence of the $\langle 110 \rangle$-oriented rods of diffuse scattering along [010] and [1$\bar{1}$0], we next characterize the temperature dependence of

the $\langle 100 \rangle$-rods of diffuse scattering along [010]. To this end, we measured q scans along the trajectory $(1,k,0)$ that pass directly through the (100) Bragg peak. As shown in Figs. 12(a)–12(c), these scans are well described by a sum of a narrow Gaussian and three Lorentzian functions of q over a broad range of temperatures. We stress that this description is by no means unique, nor should any physical significance be attributed to it or to the other fitting profiles described previously. This analysis merely provides a means by which the temperature dependence of the integrated intensity and the linewidths of the $\langle 100 \rangle$-oriented rods of diffuse scattering can be quantified. The temperature dependence of the integrated intensity of the central Lorentzian is shown in Fig. 12(d) and the diffuse scattering is observed to vanish near 320 °C. Some residual diffuse scattering remains above 320 °C as shown in Fig. 12(c), but this is effectively temperature independent and
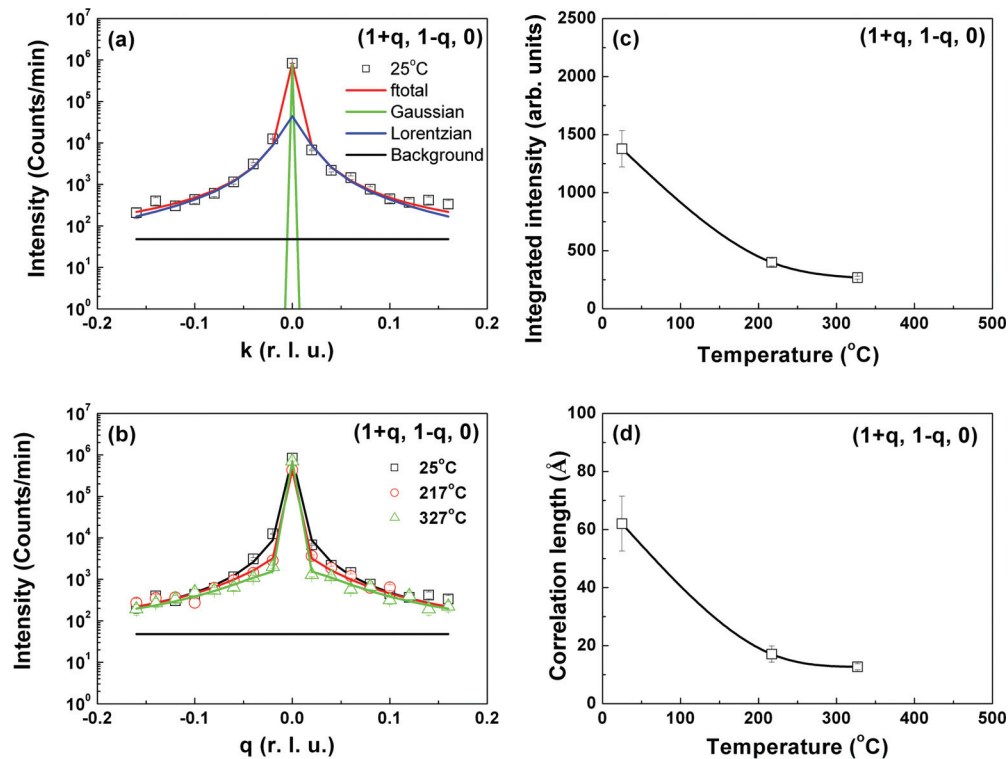
FIG. 13. (Color online) (a) Scan profile of the diffuse scattering in NBT-5.6%BT measured along $(1+q, 1-q, 0)$ near (110) at 25 °C. Solids lines represent the total (red) and individual components of the fitting profile (Gaussian, Lorentzian, and a flat, temperature-independent background). (b) Scan profiles and fits for several temperatures. Temperature dependence of the (c) integrated intensity and (d) correlation length along $[1\bar{1}0]$ associated with the Lorentzian component. All data were measured on BT9.

possibly associated with substitutional disorder. The integrated intensities of the left and right Lorentzian components are much weaker, but their temperature dependence is statistically identical to that of the central Lorentzian component (data not shown). From this, we conclude that the physical origins of the $\langle 110 \rangle$-oriented rods of diffuse scattering and those oriented along $\langle 100 \rangle$ are different because they vanish at significantly different temperatures (525 °C versus 320 °C, respectively).

E. Diffuse scattering of NBT-x%BT near the MPB

Given that the room-temperature piezoelectric properties of PMN, PZN, and NBT are all greatly enhanced when doped towards a morphotropic phase boundary (MPB) that separates pseudorhombohedral and tetragonal states, it is natural to wonder how the underlying nanoscale structure of NBT differs from the MPB composition of NBT-5.6%BT. From the contours measured at 25 °C near (100) and (110) in the (HK0) scattering plane for both compounds, shown in Figs. 7(c)–7(f), we find that the $\langle 110 \rangle$-oriented rods of diffuse scattering present in NBT are also present in NBT-5.6%BT. As before, the data in Fig. 7 are normalized to mass and counting time to facilitate direct comparison, and it is evident that the density of the contours is higher for NBT-5.6%BT along $\langle 110 \rangle$, which implies that doping towards the MPB has resulted in a longer correlation length. At the same time, the $\langle 100 \rangle$-oriented rods of diffuse scattering are substantially less prominent.

Figure 13(a) shows a single q scan measured along the trajectory $(1+q, 1-q, 0)$ that passes directly through the (110) Bragg peak for NBT-5.6%BT at 25 °C. Additional q scans at various temperatures are shown in Fig. 13(b). These intensity profiles are analogous to those shown in Fig. 11. Accordingly, they probe the short-range structural correlations along $[1\bar{1}0]$ associated with the $\langle 110 \rangle$-oriented rods of diffuse scattering in NBT-5.6%BT. As in NBT, these profiles are well described by the sum of a narrow Gaussian, a Lorentzian, and a flat, temperature-independent background. The solid lines in Fig. 13(a) show the total profile (in red) as well as the individual components. The temperature dependence of the integrated intensity and the correlation length derived from the Lorentzian component are shown in Figs. 13(c) and 13(d), respectively, and the general behavior displayed is similar to that observed in Fig. 11 for NBT. However, we note that the correlation lengths shown in Fig. 13(d) for NBT-5.6%BT are substantially larger than those in NBT. At room temperature, we observe a correlation length of the order of 60 Å along $[1\bar{1}0]$; in NBT, the same correlation length is roughly 40 Å. In addition, the q-integrated diffuse scattering near (110) in NBT-5.6%BT is more than double that for NBT. These results are summarized in Table I.

Figure 14 presents an analysis of the diffuse scattering in NBT-5.6%BT that is identical to that shown in Fig. 12 for NBT. These data probe the short-range structural correlations associated with the $\langle 100 \rangle$-oriented diffuse scattering rods. Figure 14(a) again shows a single q scan measured along the trajectory $(1,k,0)$ that passes directly through the (100) Bragg

TABLE I. Values of the correlation length $\xi(\text{Å})$ and q-integrated intensity I_0 (normalized to mass and counting time) measured at 25 °C.

		NBT (BT4)	NBT-5.6%BT (BT9)
ξ (Å)	along [1 $\bar{1}$ 0]	44 ± 1	62 ± 10
	along [010]	475 ± 15	38 ± 2
I_o	at (110)	755 ± 10	1380 ± 160
	at (100)	5050 ± 50	1960 ± 60

peak at 25 °C, while Fig. 14(b) shows profiles for several different temperatures. In this case, however, a different fitting profile was used. Unlike the three Lorentzians required for NBT, only a single Lorentzian was used along with the narrow Gaussian function to describe the (100) Bragg peak and the flat, temperature-independent background. The temperature dependence of the integrated intensity and the correlation length derived from the Lorentzian component are again shown in Figs. 14(c) and 14(d), respectively, and again the general behavior displayed is similar to that observed in Fig. 12 for NBT. But, in this case, the correlation lengths associated with the ⟨100⟩-oriented rods of diffuse scattering along [010] in NBT-5.6%BT are greatly reduced compared to those in NBT by more than a factor of 10 on doping towards the MPB, while the q-integrated intensity decreases by nearly a factor of five (see Table I). The findings presented in Figs. 13 and 14 are significant because they mirror those of Matsuura *et al.* for PMN-xPT,[36] and they therefore strongly support the ⟨110⟩-oriented rods of diffuse scattering as being not only central to relaxor behavior, but also strongly implicating the possibility that they play a central role in the ultrahigh piezoelectricity.[73]

IV. DISCUSSION

Our neutron elastic-scattering measurements show that short-range rhombohedral ($R3c$) and tetragonal ($P4bm$) correlations persist from ∼200 °C to 300 °C in the lead-free relaxor NBT. This temperature range corresponds closely to that over which a frequency-dependent dispersion is observed in the dielectric permittivity. Our results also suggest that, when viewed in combination with the x-ray data of Aksel *et al.*,[40] an anomalous skin effect is present, which has not been seen in a lead-free relaxor. Both of these structural features have been observed in the lead-based relaxor system PMN-xPT,[59–64] and together they hint at a common origin for relaxor behavior. Perhaps our most important finding is that the ⟨110⟩-oriented rods of diffuse scattering that are characteristic of lead-based, perovskite relaxors are also present in NBT. These ⟨110⟩-oriented rods of diffuse scattering exhibit the same zone dependence as in other lead-based, perovskite relaxors, but they were not observed in previous studies on NBT. They also exhibit the same dependence as those in PMN-xPT when doped close to the morphotropic phase
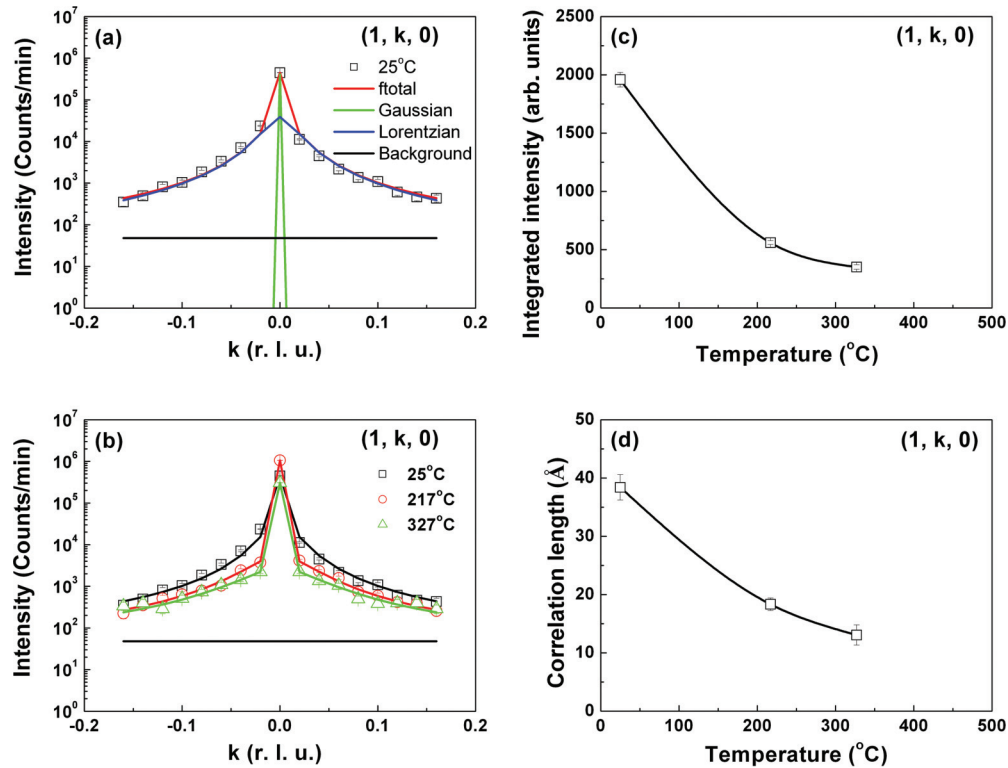

FIG. 14. (Color online) (a) Scan profile of the diffuse scattering in NBT-5.6%BT measured along $(1,k,0)$ near (100) at 25 °C. Solids lines represent the total (red) and individual components of the fitting profile (Gaussian, Lorentzian, and a flat, temperature-independent background). (b) Scan profiles and fits for several temperatures. Temperature dependence of the (c) integrated intensity and (d) correlation length along [010] associated with the Lorentzian component. All data were measured on BT9.

boundary. This strongly suggests that the underlying nanoscale structure associated with the ⟨110⟩-oriented rods of diffuse scattering could be common to all perovskite relaxors. These similarities may seem surprising at first glance because of the differences between the *A*-site cations Na^+ and Pb^{2+}, the latter of which carries a lone pair of electrons. However, a recent neutron PDF study of $NaNbO_3$ by Jiang *et al.*[74] also reports the persistence of rhombohedral $R3c$ correlations spanning a large temperature range like those in NBT. In addition, $NaNbO_3$ exhibits relaxorlike behavior because of the off-centering of the Na^+ cations. Thus, it seems that Na and Pb behave in a similar manner in these oxide perovskite relaxors. We, therefore, believe that the anisotropic, temperature-dependent diffuse scattering exhibited by PMN and other lead-based relaxors, and in NBT as well, is a relaxor-specific property, and that it may also be associated with the ultrahigh piezoelectric response. We finally speculate that strong random electric fields are the driving force behind the relaxor-specific diffuse scattering insofar as we see no evidence of comparable diffuse scattering in two homovalent perovskite materials, KLT 5% and KTN 5%, both of which have been reported as relaxors in the literature.[65–67]

*wenweige@vt.edu

[1] G. A. Smolenskii, V. A. Isupov, A. I. Agranovskaya, and N. N. Krainik, Fiz. Tverd. Tela (Leningrad) **2**, 2982 (1960) [Sov. Phys. Solid State **2**, 2651 (1960)].

[2] Y. M. Chiang, G. W. Farrey, and A. N. Soukhojak, Appl. Phys. Lett. **73**, 3683 (1998).

[3] T. Takenaka, K. Maruyama, and K. Sakata, Jpn. J. Appl. Phys. **30**, 2236 (1991).

[4] Q. H. Zhang, Y. Y. Zhang, F. F. Wang, Y. J. Wang, D. Lin, X. Y. Zhao, H. S. Luo, W. W. Ge, and D. Viehland, Appl. Phys. Lett. **95**, 102904 (2009).

[5] T. Takenaka, H. Nagata, and Y. Hiruma, IEEE Trans. Ultrason. Ferr. **56**, 1595 (2009).

[6] Y. Guo, Y. Liu, R. L. Withers, F. Brink, and H. Chen, Chem. Mater. **23**, 219 (2011).

[7] W. Jo, J. E. Daniels, J. L. Jones, X. Tan, P. A. Thomas, D. Damjanovic, and J. R. Rödel, J. Appl. Phys. **109**, 014110 (2011).

[8] Y. Guo, M. Gu, H. Luo, Y. Liu, and R. L. Withers, Phys. Rev. B **83**, 054118 (2011).

[9] S. E. Park and T. R. Shrout, J. Appl. Phys. **82**, 1804 (1997).

[10] L. E. Cross, Ferroelectrics **151**, 305 (1994).

[11] Y. P. Guo, H. S. Luo, D. Ling, H. Q. Xu, T. H. He, and Z. W. Yin, J. Phys.: Condens. Matter **15**, L77 (2003).

[12] I. K. Jeong, T. W. Darling, J. K. Lee, T. Proffen, R. H. Heffner, J. S. Park, K. S. Hong, W. Dmowski, and T. Egami, Phys. Rev. Lett. **94**, 147602 (2005).

[13] B. Dkhil, J. M. Kiat, G. Calvarin, G. Baldinozzi, S. B. Vakhrushev, and E. Suard, Phys. Rev. B **65**, 024104 (2001).

[14] P. M. Gehring, S. Wakimoto, Z. G. Ye, and G. Shirane, Phys. Rev. Lett. **87**, 277601 (2001).

[15] P. M. Gehring, S. E. Park, and G. Shirane, Phys. Rev. Lett. **84**, 5216 (2000).

[16] G. Burns and F. H. Dacol, Solid State Commun. **48**, 853 (1983).

[17] H. You and Q. M. Zhang, Phys. Rev. Lett. **79**, 3950 (1997).

[18] N. Takesue, Y. Fuji, and H. You, Phys. Rev. B **64**, 184112 (2001).

[19] D. La-Orauttapong, J. Toulouse, Z. G. Ye, W. Chen, R. Erwin, and J. L. Robertson, Phys. Rev. B **67**, 134110 (2003).

[20] H. Hiraka, S. H. Lee, P. M. Gehring, G. Y. Xu, and G. Shirane, Phys. Rev. B **70**, 184105 (2004).

[21] G. Y. Xu, Z. Zhong, H. Hiraka, and G. Shirane, Phys. Rev. B **70**, 174109 (2004).

[22] G. Y. Xu, Z. Zhong, Y. Bing, Z. G. Ye, and G. Shirane, Nat. Mater. **5**, 134 (2006).

[23] G. Y. Xu, J. S. Wen, C. Stock, and P. M. Gehring, Nat. Mater. **7**, 562 (2008).

[24] P. M. Gehring, H. Hiraka, C. Stock, S. H. Lee, W. Chen, Z. G. Ye, S. B. Vakhrushev, and Z. Chowdhuri, Phys. Rev. B **79**, 224109 (2009).

[25] K. Hirota, Z. G. Ye, S. Wakimoto, P. M. Gehring, and G. Shirane, Phys. Rev. B **65**, 104105 (2002).

[26] G. Y. Xu, G. Shirane, J. R. D. Copley, and P. M. Gehring, Phys. Rev. B **69**, 064112 (2004).

[27] C. Stock, R. J. Birgeneau, S. Wakimoto, J. S. Gardner, W. Chen, Z. G. Ye, and G. Shirane, Phys. Rev. B **69**, 094104 (2004).

[28] S. Vakhrushev, A. Ivanov, and J. Kulda, Phys. Chem. Chem. Phys. **7**, 2340 (2005).

[29] A. Cervellino, S. N. Gvasaliya, O. Zaharko, B. Roessli, G. M. Rotaru, R. A. Cowley, S. G. Lushnikov, T. A. Shaplygina, and M. T. Fernandez-Diaz, J. Appl. Crystallogr. **44**, 603 (2011).

[30] T. R. Welberry and D. J. Goossens, Acta Crystallogr. A **64**, 23 (2008).

[31] T. R. Welberry, D. J. Goossens, and M. J. Gutmann, Phys. Rev. B **74**, 224108 (2006).

[32] M. Paściak, M. Wołcyrz, and A. Pietraszko, Phys. Rev. B **76**, 014117 (2007).

[33] T. R. Welberry and D. J. Goossens, J. Appl. Crystallogr. **41**, 606 (2008).

[34] P. Ganesh, E. Cockayne, M. Ahart, R. E. Cohen, B. Burton, R. J. Hemley, Y. Ren, W. G. Yang, and Z. G. Ye, Phys. Rev. B **81**, 144102 (2010).

[35] A. Bosak, D. Chernyshov, S. Vakhrushev, and M. Krisch, Acta Crystallogr. A **68**, 117 (2012).

[36] M. Matsuura, K. Hirota, P. M. Gehring, Z. G. Ye, W. Chen, and G. Shirane, Phys. Rev. B **74**, 144107 (2006).

[37] G. O. Jones and P. A. Thomas, Acta Crystallogr. B **56**, 426 (2000).

[38] G. O. Jones and P. A. Thomas, Acta Crystallogr. B **58**, 168 (2002).

[39] S. Gorfman and P. A. Thomas, J Appl Crystallogr. **43**, 1409 (2010).

[40] E. Aksel, J. S. Forrester, J. L. Jones, P. A. Thomas, K. Page, and M. R. Suchomel, Appl. Phys. Lett. **98**, 152901 (2011).

[41] I. P. Aleksandrova, Y. N. Ivanov, A. A. Sukhovskii, and S. B. Vakhrushev, Phys. Solid State **48**, 1120 (2006).

[42] J. Kreisel, P. Bouvier, B. Dkhil, P. A. Thomas, A. M. Glazer, T. R. Welberry, B. Chaabane, and M. Mezouar, Phys. Rev. B **68**, 014113 (2003).

[43] I. P. Aleksandrova, A. A. Sukhovsky, Y. Ivanov, Y. Yablonskaya, and S. B. Vakhrushev, Ferroelectrics **378**, 16 (2009).

[44] P. A. Thomas, S. Trujillo, M. Boudard, S. Gorfman, and J. Kreisel, Solid State Sci. **12**, 311 (2010).

[45] M. Matsuura, H. Iida, K. Hirota, K. Ohwada, Y. Noguchi, and M. Miyayama, Phys. Rev. B **87**, 064109 (2013).

[46] Q. H. Zhang, Y. Y. Zhang, F. F. Wang, D. Lin, X. B. Li, X. Y. Zhao, and H. S. Luo, J. Cryst. Growth **312**, 457 (2010).

[47] C. S. Tu, I. G. Siny, and V. H. Schmidt, Phys. Rev. B **49**, 11550 (1994).

[48] V. A. Isupov and T. V. Kurzina, Izv. AN SSSR, Ser. Fiz. **47**, 616 (1983) [Sov. Phys.: Bull. Acad. Sci. USSR, Phys. Ser. **47**, 194 (1983)].

[49] L. E. Cross, Ferroelectrics **76**, 241 (1987).

[50] D. Viehland, S. J. Jang, L. E. Cross, and M. Wuttig, Phys. Rev. B **46**, 8003 (1992).

[51] S. B. Vakhrushev, B. E. Kvyatkovskii, N. M. Okuneva, E. L. Plachenova, and P. P. Syrnikov, Pis'ma Zh. Eskp. Teor. Fiz. **35**, 111 (1982); S. B. Vakhrushev, V. A Isupov, B. E. Kvyatkovsky, N. M. Okuneva, I. P. Pronin, G. A. Smolensky, and P. P. Syrnikov, Ferroelectrics **63**, 153 (1985).

[52] A. Glazer, Acta Crystallogr. Sect. B **28**, 3384 (1972).

[53] I. P. Swainson, C. Stock, P. M. Gehring, G. Xu, K. Hirota, Y. Qiu, H. Luo, X. Zhao, J.-F. Li, and D. Viehland, Phys. Rev. B **79**, 224301 (2009).

[54] G. Shirane, S. M. Shapiro, and J. M. Tranquada, *Neutron Scattering with a Triple-Axis Spectrometer* (Cambridge University Press, Cambridge, UK, 2002).

[55] D. Phelan, X. Long, Y. Xie, Z. G. Ye, A. M. Glazer, H. Yokota, P. A. Thomas, and P. M. Gehring, Phys. Rev. Lett. **105**, 207601 (2010).

[56] A. M. Balagurov, E. Yu. Koroleva, A. A. Naberezhnov, V. P. Sakhnenko, B. N. Savenko, N. V. Ter-Oganessian, and S. B. Vakhrushev, Phase Transitions **79**, 163 (2006).

[57] B. N. Rao, A. N. Fitch, and R. Ranjan, Phys. Rev. B **87**, 060102(R) (2013).

[58] I. Levin and I. M. Reaney, Adv. Funct. Mater. **22**, 3445 (2012).

[59] G. Y. Xu, Z. Zhong, Y. Bing, Z. G. Ye, C. Stock, and G. Shirane, Phys. Rev. B **67**, 104102 (2003).

[60] G. Y. Xu, H. Hiraka, G. Shirane, and K. Ohwada, Appl. Phys. Lett. **84**, 3975 (2004).

[61] G. Y. Xu, D. Viehland, J. F. Li, P. M. Gehring, and G. Shirane, Phys. Rev. B **68**, 212410 (2003).

[62] G. Xu, P. M. Gehring, C. Stock, and K. Conlon, Phase Transitions **79**, 135 (2006).

[63] P. M. Gehring, W. Chen, Z. G. Ye, and G. Shirane, J. Phys.: Condens. Matter **16**, 7113 (2004).

[64] K. H. Conlon, H. Luo, D. Viehland, J. F. Li, T. Whan, J. H. Fox, C. Stock, and G. Shirane, Phys. Rev. B **70**, 172204 (2004).

[65] G. A. Samara, J. Phys.: Condens. Matter **15**, R367 (2003).

[66] S. Wakimoto, G. A. Samara, R. K. Grubbs, E. L. Venturini, L. A. Boatner, G. Xu, G. Shirane, and S.-H. Lee, Phys. Rev. B **74**, 054101 (2006).

[67] J. Toulouse, Ferroelectrics **369**, 203 (2008).

[68] J. S. Wen, G. Y. Xu, C. Stock, P. M. Gehring, Z. Zhong, L. A. Boatner, E. L. Venturini, and G. A. Samara, Phys. Rev. B **78**, 144202 (2008).

[69] C. Stock, *et al.*, Phys. Rev. B **73**, 064107 (2006).

[70] B. Mihailova, *et al.*, Phys. Rev. Lett. **101**, 017602 (2008).

[71] E. Matsubara and J. B. Cohen, Acta Metall. Mater. **33**, 1945 (1985).

[72] J. Kreisel, P. Bouvier, B. Dkhil, B. Chaabane, A. M. Glazer, P. A. Thomas, and T. R. Welberry, Ferroelectrics **302**, 293 (2004).

[73] P. M. Gehring, J. Adv. Dielectr. **02**, 1241005 (2012).

[74] L. Jiang, D. C. Mitchell, W. Dmowski, and T. Egami, Phys. Rev. B **88**, 014105 (2013).